Department of Applied Physics

Gyrokinetic full-f transport simulations of ohmic FT-2 tokamak discharges

Susan Leerink

Aalto University

DOCTORAL DISSERTATIONS

Aalto University publication series
DOCTORAL DISSERTATIONS 176/2012

Gyrokinetic full-f transport simulations of ohmic FT-2 tokamak discharges

Susan Leerink

A doctoral dissertation completed for the degree of Doctor of Science to be defended, with the permission of the Aalto University School of Science, at a public examination held at the Auditorium of the engineering physics building on 21 December 2012 at 12.

Aalto University
School of Science
Department of Applied Science
Fusion and Plasma physics

Supervising professor
Prof. Rainer Salomaa

Thesis advisor
Dr. Jukka Heikkinen

Preliminary examiners
Dr. Yanick Sarazin, CEA-IFRM, Centre de Cadarache, France
Dr. Garrard Conway, Max-Planck Institut fur Plasmaphysik, Germany

Opponents
Prof. Tünde Fülöp,Chalmers University of Technology, Sweden

Aalto University publication series
DOCTORAL DISSERTATIONS 176/2012

ISBN 978-952-60-4935-9 (printed)
ISBN 978-952-60-4936-6 (pdf)
ISSN-L 1799-4934
ISSN 1799-4934 (printed)
ISSN 1799-4942 (pdf)
http://urn.fi/URN:ISBN:978-952-60-4936-6

Unigrafia Oy
Helsinki 2012

Finland

441 697
Printed matter

Aalto University

Abstract

Aalto University, P.O. Box 11000, FI-00076 Aalto www.aalto.fi

Author
Susan Leerink

Name of the doctoral dissertation
Gyrokinetic full-f transport simulations of ohmic FT-2 tokamak discharges

Publisher School of Science

Unit Department of Applied Physics

Series Aalto University publication series DOCTORAL DISSERTATIONS 176/2012

Field of research Fusion and Plasma Physics

Manuscript submitted 12 June 2012 **Date of the defence** 21 December 2012

Permission to publish granted (date) 14 November 2012 **Language** English

☐ **Monograph** ☒ **Article dissertation (summary + original articles)**

Abstract

The work described in the thesis focuses on understanding large-scale mean ExB flows, fine-scale zonal flows and turbulent transport in ohmic plasma discharges in the small Russian FT-2 tokamak from a first principal basis. The investigations are performed with the full-f particle-in-cell (PIC) code Elmfire which calculates the time evolution of the full distribution function of the electrons and a selection of ions while self-consistently calculating the electric field making the code suitable to study neoclassical and turbulent transport processes simultaneously.

The equations solved in the Elmfire code are based on a set of gyrokinetic Vlasov equations which explicitly includes the polarization drift in the equations of motion by using an alternative definition for the gyrocenter. The differences to the standard gyrokinetic model and the advantages of this treatment for particle-in-cell codes are addressed. The coefficient matrix for the Poisson equation is constructed implicitly from the ion polarization and the electron parallel nonlinearity. Two types of interpolation schemes to obtain the particle electric field from the grid are implemented in the Elmfire code and their influence on the particle transport and momentum conservation are discussed. Collisions are treated by a binary collision model. The dependence of the transport quantities on the spatial resolution and the influence of particle noise are addressed. Steady state simulation profiles are obtained by the balance of ohmic heating and particle/energy transport, radiation losses and energy transported to a limiter surface.

Direct measurements of transport phenomena in ohmic FT-2 discharges are shown to be quantitatively reproduced by the Elmfire simulation predictions. A detailed agreement with mean equilibrium ExB flows, oscillating fine-scale zonal flows and turbulence spectra observed by a set of sophisticated microwave back-scattering techniques as well as a good fit of the thermal diffusivity data are demonstrated. The measured and simulated mean equilibrium ExB flows are validated against various analytical models where the effect of the T_e/T_i ratio, ion orbit losses and impurities are investigated in more detail. Statistical analysis of the oscillating fine-scale zonal flow are presented and a comparison to geodesic acoustic mode statistics while including the impurity contribution is performed

Keywords Energy, Nuclear Fusion, Plasma physics, Tokamak, Transport, Turbulence, Gyrokinetics, Computational Physics

ISBN (printed) 978-952-60-4935-9 **ISBN (pdf)** 978-952-60-4936-6

ISSN-L 1799-4934 **ISSN (printed)** 1799-4934 **ISSN (pdf)** 1799-4942

Location of publisher Espoo **Location of printing** Espoo **Year** 2012

Pages 134 **urn** http://urn.fi/URN:ISBN:978-952-60-4936-6

Preface

The work presented in this thesis has been carried out at the Department of applied physics of the Aalto University between 2006 and 2012. When I started to work on my thesis in the Elmfire code development group in 2006, Dr. Jukka Heikkinen, Dr. Timo Kiviniemi and Salomon Janhunen already spent 6 long years on developing and benchmarking the code against neoclassical theory and other gyrokinetic codes. Although only limited computational resources were available at the time, it was decided that experimental validation of the Elmfire code would be the next step. Due to its small size, its geographical location and a long history of mutual collaboration, the Russian FT-2 tokamak experiment in St. Petersburg was chosen to be the appropriate tokamak to start this effort. In the next paragraphs I would like to show my appreciation to all the persons that have helped me to construct this thesis over the past six years.

I would like to start with thanking my instructor Dr. Jukka Heikkinen and Dr. Timo Kiviniemi for their guidance during the work and for critically reading this manuscript. It has been and still is a great privilege to work with both of you. I am indebted to Salomon Janhunen and Dr. Francisco Ogando for their fantastic introduction to the Elmfire code and for many useful discussions. They have been of tremendous help while carrying out my thesis work. Furthermore this thesis would not have been possible without the support of the entire FT-2 tokamak team, where I specially would like to thank Prof. Evgeniy Gusakov, Dr. Alexey Gurchenko, Dr. Victor Bulanin and Dr. Serguey Lashkul for their contributions. I would also like to thank Dr. Peter Catto, Prof. Felix Parra, Dr. Seong-Hoe Ku and Prof. C.S. Chang for sharing their valuable insights during my stay at MIT and NYU in 2009.

I am thankful to Prof. Rainer Salomaa for giving me the opportunity to work within his research group. His moral support during the last stages of writing the thesis was also greatly appreciated. Furthermore I would like to thank all

my colleagues at Aalto University and VTT for many pleasant conversations during lunches, coffee breaks and other encounters. You have made me feel very welcome and at home.

On a more personal note, I would like to thank my family for their many trips to Finland and for their hospitality when I come over for a visit. I am very fortunate to have such a supportive group of people back home! Last but not least I would like to thank my husband Rob for his continuous love and support and for always keeping my morale high.

The work in this thesis has been carried out within the Euratom-Tekes association agreement. Financial support from the Finnish Academy is gratefully acknowledged.

Espoo, November 22, 2012,

Susan Leerink

Contents

List of Publications

This thesis consists of an overview and of the following publications which are referred to in the text by their Roman numerals.

I S.J. Janhunen, F. Ogando, J.A. Heikkinen, T.P. Kiviniemi and S. Leerink. Collisional dynamics of E_r in turbulent plasmas in toroidal geometry. *Nuclear Fusion*, 47, 285, July 2007.

II S. Leerink, J.A. Heikkinen, S.J. Janhunen, T.P. Kiviniemi, M. Nora and F. Ogando. Gyrokinetic full-f analysis of electric field dynamics and poloidal velocity in the FT2-tokamak configuration. *Plasma Physics Reports*, 34,716, May 2008.

III S. Leerink, V.V. Bulanin, E.Z. Gusakov, J.A. Heikkinen, S.J. Janhunen, T.P. Kiviniemi, T. Korpilo, M. Nora and F. Ogando. Synthetic Doppler Reflectometer Diagnostic for Nonlinear Global Gyrokinetic Simulations. *Contributions to Plasma Physics* , 50, 242, May 2010.

IV A.D. Gurchenko, E.Z. Gusakov, D.V. Kouprienko, S. Leerink, A.B. Altukhov, J.A. Heikkinen, S.I. Lashkul, L.A. Esipov and A.Yu. Stepanov. Observation of turbulence exponential wave number spectra at ion sub-Larmor scales in FT-2 tokamak. *Plasma Phys. Control. Fusion*, 52, 035010, February 2010.

V S. Leerink, F.I. Parra and J.A. Heikkinen. Comment on "Nonlinear gyrokinetic theory with polarization drift". *Physics of Plasmas*, 7, 124701, December 2010.

VI J.A. Heikkinen, S.J. Janhunen, T.P. Kiviniemi, T. Korpilo, S. Leerink and F. Ogando. Interpolation for momentum conservation in 3D toroidal gyrokinetic particle simulation of plasmas. *Computer Physics Communications*, 183, 1719, March 2012.

VII S. Leerink, V.V. Bulanin, A.D. Gurchenko, E.Z. Gusakov, J.A. Heikkinen, S.J. Janhunen, A.B. Altukhov, L.A. Esipov, M.Yu. Kantor, T.P. Kiviniemi, T. Korpilo, D.V. Kuprienko, S.I. Lashkul and A.V. Petrov. Multi-scale investigations of drift wave turbulence and plasma flows: Measurements and full-f gyrokinetic simulations. *Physics Review Letters*, 109, 165001, October 2012.

VIII T.P. Kiviniemi, S. Leerink, J.A. Heikkinen, S. Janhunen and T. Korpilo. Gyrokinetic simulations of the edge pedestal in the TEXTOR tokamak. *Contributions to Plasma Physics*, 52, 406, June 2012.

Author's Contribution

Publication I: "Collisional dynamics of E_r in turbulent plasmas in toroidal geometry"

In this publication the first Elmfire simulation results of the radial electric field dynamics in the presence of micro turbulence for simplified FT-2 tokamak parameters are presented and different sources producing deviations of the radial electric field in regard to the analytical neoclassical estimates are discussed. The author contributed to the paper by developing diagnostic packages for the correlation, spectral and poloidal velocity analysis. Although those analysis are not included explicitly in the paper, they were included in the reply to the referee as a proof that the simulation had reached the turbulent saturated state.

Publication II: "Gyrokinetic full-f analysis of electric field dynamics and poloidal velocity in the FT2-tokamak configuration"

A similar radial electric field analysis as in publication I with more realistic FT-2 tokamak parameters is presented. Clear geodesic acoustic mode activity is observed in the radial electric field time trace. Furthermore convergence of the simulation is investigated by studying the time development of the turbulence k-spectra. The two main contributors to the poloidal velocity, the phase velocity and the $E_r \times B$ velocity, are presented and a link to Doppler reflectometer measurements is made. The author wrote the full paper and produced all the figures.

Publication III: "Synthetic Doppler Reflectometer Diagnostic for Nonlinear Global Gyrokinetic Simulations"

The author investigated a method to validate poloidal velocity of density fluctuations simulated with the ELMFIRE code to Doppler reflectometry measurements. A proof of principle is given and an investigation into the poloidal rotation of density fluctuations is performed. The author programmed the synthetic diagnostic for the Elmfire code, performed the simulations, wrote the full paper and produced all the figures.

Publication IV: "Observation of turbulence exponential wave number spectra at ion sub-Larmor scales in FT-2 tokamak"

In this work the experimental observations of turbulence wave-number spectra obtained with the enhanced scattering diagnostic at the FT-2 tokamak are presented. The author contributed to the theoretical explanation of the measurements by performing the linear growth rate and frequency analysis of unstable drift modes with the gyrokinetic GS2 code presented in figure 6 a&b.

Publication V: "Comment on "Nonlinear gyrokinetic theory with polarization drift""

In 2010 questions concerning the validity of the theoretical background of the Elmfire code arose within the gyrokinetic community. While the author was visiting the Massachusetts Institute of Technology in 2009 these same questions had come up during discussions with Prof. F.I. Parra. At the time a clarification was found by accounting for the different definition of the distribution function while sampling particles with the particle-in-cell method. The comment to previously published material on the gyrokinetic model adapted in the Elmfire code is written by the author in collaboration with Prof. F.I. Parra.

Publication VI: "Interpolation for momentum conservation in 3D toroidal gyrokinetic particle simulation of plasmas"

After the authors visit to the Massachusetts Institute of Technology in 2009, a group effort to optimize the toroidal angular momentum conservation in the

Elmfire code was lounched. As a result a new and better toroidal angular momentum conserving interpolation scheme for the electric field was developed. The author contributed to this publication by studying several interpolation stencils for the inversion of the coefficient matrix by programming a simplified 2D matrix inversion code.

Publication VII: "Multi-scale investigations of drift wave turbulence and plasma flows: Measurements and full-f gyrokinetic simulations"

The author used the Elmfire code to validate various transport properties by means of the synthetic diagnostic presented in publication III, heat conductivity as well as the radial electric field dynamics. It was proven that Elmfire simulations of a ohmic FT-2 discharge quantitatively reproduce estimations of the effective thermal diffusivities and the mean poloidal fluctuation rotation profile, the GAM dynamics and E_r fluctuation statistics and the DR frequency spectra demonstrating the codes ability to simultaneously reproduce a wide range of transport scale levels accurately. The author studied the steady state simulation profiles by balancing the ohmic heating and particle/energy transport, radiation losses and particle losses transported to a limiter surface. The author wrote the full paper and produced all the figures included in the paper.

Publication VIII: "Gyrokinetic simulations of the edge pedestal in the TEXTOR tokamak"

Ongoing ELMFIRE simulation work on transport studies in TEXTOR low and high confiment discharges are addressed by presenting the radial electric field, heat conductivity and particle fluxes. The author performed a substantial part of the data analysis presented in this article and produced figures 1a&b, 2a&b, 3, 4b and 6a&b.

1. Introduction

With the worlds energy consumption steadily increasing every year the need for new and clean energy sources is growing rapidly. Nuclear fusion as a basis for large scale commercial energy production could offer these prospects in the near future. It is the same energy source that powers the sun by fusing light atomic nuclei together thereby releasing a large amount of energy. This process produces no long term radioactive waste, is safe and has no emission of greenhouse gases. With hydrogen isotopes as its fuel, the available fuel resources can meet the world's energy requirement for thousands of years. For fusion reactions to occur on earth, fuel particles must reach temperatures of several hundred million degrees Celsius for sufficiently long time for the fuel particles to overcome the repulsive coulomb force and fuse. The higher the cross-section the easier particles will fuse and promising candidates for fusion reactions on earth are:

$$^2\mathrm{D} + {}^2\mathrm{D} \rightarrow {}^3\mathrm{T} + n + 4.03\ \mathrm{MeV} \qquad 50\% \qquad (1.1)$$

$$\rightarrow {}^3\mathrm{He} + n + 3.27\ \mathrm{MeV} \qquad 50\% \qquad (1.2)$$

$$^2\mathrm{D} + {}^3T \rightarrow {}^4\mathrm{He} + n + 17.6\ \mathrm{MeV} \qquad (1.3)$$

At fusion temperatures charged electrons are no longer attached to the atoms and an ionized gas, called a plasma, is created. Sustaining a high temperature plasma on earth is a very difficult task. This is mainly due to the fact that there are no materials able to store the plasma without melting and an extra barrier is needed that prevents the plasma of coming in to contact with the walls of its container. The most promising device for creating this barrier is the tokamak which uses magnetic fields to confine the plasma. The tokamak exploits the fact that charged particles follow a helical path along the magnetic field lines. By bending the magnetic field lines into a closed loop the plasma is confined and fusion reactions can continue as long as there is enough fuel available. In the tokamak device a poloidal and toroidal magnetic field is

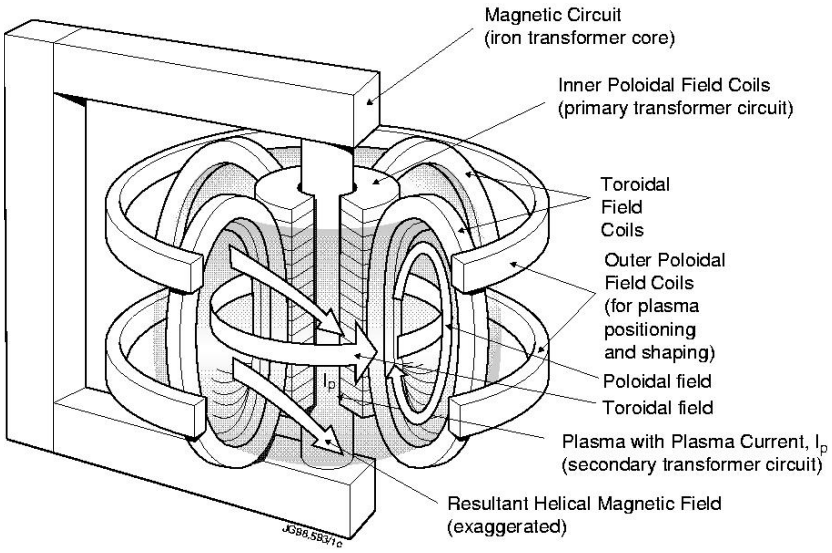

Figure 1.1. Simplified schematic picture of the tokamak [1]

generated, which makes the plasma particles to run around in spirals without touching the wall of the chamber, as illustrated in figure 1.1.

Although experimental research on tokamak devices already started several decades ago, perfectly controlled nuclear fusion has not yet been achieved. A major obstacle is that the transport of the fuel particles across the magnetic field lines can not be predicted by only analytical transport theory. Turbulence induced transport, a still unsolved problem in physics in general, has been attributed to be the main reason. It is causing fuel particles to drift faster from the magnetic field lines, disturbing the plasma confinement and thereby the fusion process. Turbulent transport has been found dominant in tokamak experiments where in particular the electron heat conductivity has been measured to be one to two magnitudes higher than the neoclassical predictions. Although turbulence is responsible for degrading the overall radial confinement of the plasma, experimentalists have found several enhanced confinement regimes where the transport caused by anomalous turbulence was decreased remarkably. It is widely believed that low frequency turbulence-induced zonal flows along with large $E \times B$ flows is decorrelating turbulent fluctuations and decreasing the radial correlation length of turbulent fluctuations leading to a radial transport bifurcation. Obtaining a better understanding of turbulent transport and in particular its self regulation would be a crucial step forward towards achieving reactor relevant tokamak plasmas.

Turbulence induced transport is a transport regime characterized by chaotic

property changes, and investigations into this regime can be done by so-called first principal computer models. These codes solve the coupled problem of Bolzmann's kinetic equations for the total particle distribution (full-f) function and Maxwell's equations in a complex magnetic field while using the gyrokinetic model. The gyrokinetic model performs averaging over the gyro-orbit reducing the calculations from six-dimensional space to five dimensions while keeping the time and length resolutions high enough for turbulence studies. During the last decades the computational capacity reached the level with which modeling of turbulence induced transport in tokamak experiments with the gyrokinetic approach has become possible [2-17].

1.1 Single particle motion in a tokamak

Particle and heat transport in a cylindrical plasma configuration with homogeneous and stationary magnetic field can be described by simple Coulomb collisions between particles. The diffusion coefficients can be obtained by a random walk model $D_\alpha = \rho_\alpha^2/\tau$, with τ the collision time and ρ_α the random walk step size of particle species α defined by its Larmor radius. When a plasma, however, is bent in a torus shape, like in a tokamak, the magnetic field is no longer homogeneous and the curvature and gradient of the magnetic field will create extra drifts usually increasing the transport compared to the classical random walk model. Collisional transport including these extra drifts is described by neoclassical transport. One of the most visible aspect of neoclassical transport is the presence of trapped particles. Particles traveling in a magnetic field gradient $\nabla_\parallel B$ will experience a force $F_\parallel = \mu \nabla_\parallel B$, where $\mu = m_\alpha v_\perp^2/2B$ is a constant of motion called the magnetic moment, where m_α is the species mass and $v_\perp$ the perpendicular velocity. This force will slow down the parallel motion of the particles when they are moving to the high field side of the tokamak and in the absence of collisions a fraction of the total amount of particles will have low enough $v_\parallel$ to be stopped and reflected back. These particles will oscillate in the weak magnetic field region of the tokamak on so called banana orbits with a bounce frequency $\omega_b = v_{th}/(qR_o)$, where v_{th} is the thermal velocity, q the safety factor and R_0 the major radius of the tokamak. The remaining part of the particles with high enough velocity to overcome this reflection are called passing particles. Due to drifts the orbits of the passing and trapped particles will be shifted compared to the magnetic field lines where the shift for the trapped particles is called the banana orbit width $w_B \propto \rho_\alpha q$. An estimate for the fraction of particles trapped in banana

orbits is given by [35]:

$$f_t = \frac{1-(1-\epsilon)^2\sqrt{1-\epsilon^2}}{1+1.46\sqrt{\epsilon}} \tag{1.4}$$

with $\epsilon = r/R_0$ the inverse aspect ratio at radial position r. The existence of particles on shifted orbits can have a significant impact on the particle and heat transport. When a particle experiences a collision in the time that it needs to complete one orbit, the particle will not be able of finish one orbit and the transport will be close to the classical transport. When the collision frequency however is lower than the bounce frequency, the particle is able to complete an orbit and the step size in the random walk model will no longer be the Larmor radius but the much larger banana width, resulting in higher particle and heat transport. Standard neoclassical transport theory defines three transport regimes depending on the ratio between the ion bounce frequency and the ion collision frequency $\nu_* = \nu_{ii}/\omega_b\epsilon^{-3/2}$ where $\nu_{ii} = q_i^4 n_i \lambda_{ii}/(4\pi\varepsilon_0^2 m_i^2 v_{th}^3)$ is the ion-ion collsion frequency with n_i, m_i and q_i the ion density, mass and charge, respectively, λ_{ii} the coulomb logarithm and ε_0 the vacuum permittivity. In the low collisional banana regime ($\nu_* < 1$) passing and trapped particle orbits exist, in the highly collisional Pfirsch-Schluter regime ($\nu_* > \epsilon^{-3/2}$) particles do not complete full orbits and in the intermediate plateau regime($1 < \nu_* < \epsilon^{-3/2}$) only passing orbits are present. For every collision regime various neoclassical theories have been developed to estimate the heat and particle fluxes while taking various assumptions on for example the magnetic field background, the flow velocity, the collision operator, etc.

1.2 A set of fluid equations

The collective statistical behavior of a large number of charged particle in a plasma is governed by the Fokker Planck equation

$$\frac{\partial f_\alpha}{\partial t} + \mathbf{v}\cdot\nabla f_\alpha + \frac{q_\alpha}{m_\alpha}(\mathbf{E}+\mathbf{v}\times\mathbf{B})\frac{\partial f_\alpha}{\partial \mathbf{v}} = C_\alpha(f) \tag{1.5}$$

which describes the change of the distribution function $f_\alpha(\mathbf{x},\mathbf{v},t)$ of a single species α as a result of the Lorentz force $\mathbf{F} = q_\alpha(\mathbf{E}+\mathbf{v}\times\mathbf{B})$ and collisions $C_\alpha(f)$. Here $\mathbf{E}$ is the electric field, $\mathbf{B}$ the magnetic field, q_α the particle charge, $\mathbf{x}$ the location in the configuration space and $\mathbf{v}$ the velocity vector. A full kinetic description of the transport processes in a plasma is obtained by solving equation 1.5 together with Maxwell equations:

$$\nabla \times \mathbf{E} = -\frac{\partial \mathbf{B}}{\partial t} \tag{1.6}$$

$$\nabla \times \mathbf{B} = \mu_0 \mathbf{j} + \mu_0 \varepsilon_0 \frac{\partial \mathbf{E}}{\partial t} \tag{1.7}$$

$$\nabla \cdot \mathbf{B} = 0 \tag{1.8}$$

$$\nabla \cdot \mathbf{E} = \frac{\rho_c}{\varepsilon_0} \tag{1.9}$$

while appropriately accounting for the collisions. Here $\mathbf{j}$ is the electric current density, ρ_c the electric charge density and μ_0 the vacuum permeability. When the plasma is assumed to be in an equilibrium state a set of fluid equations for macroscopic quantities can be constructed by taking moments of the distribution function. In the absence of sources and sinks for particles, momentum and energy the moments for density n_α, flow velocity $\mathbf{v}_\alpha$ and temperature T_α are expressed by [18]:

$$\frac{dn_\alpha}{dt} + n_\alpha \nabla \cdot \mathbf{v}_\alpha = 0 \tag{1.10}$$

$$n_\alpha m_\alpha \frac{d\mathbf{v}_\alpha}{dt} = n_\alpha q_\alpha (\mathbf{E} + \mathbf{v}_\alpha \times \mathbf{B}) - \nabla \cdot \mathbf{P}_\alpha + \mathbf{R}_\alpha \tag{1.11}$$

$$\frac{3}{2} n_\alpha \frac{d}{dt} T_\alpha + p_\alpha \nabla \cdot \mathbf{v}_\alpha = -\nabla \cdot \mathbf{q}_\alpha - (\mathbf{\Pi} \cdot \nabla) \cdot \mathbf{v}_\alpha + \sum_{\alpha=\beta} Q_{\alpha\beta} \tag{1.12}$$

where

$$\frac{d}{dt} = \frac{\partial}{\partial t} + \mathbf{v}_\alpha \cdot \nabla \tag{1.13}$$

is the time derivative in the frame moving at the fluid velocity $\mathbf{v}_\alpha$, also referred to as the convective derivative. Here $\mathbf{R}_\alpha$ is the inter species friction force and $\mathbf{P}_\alpha$ the pressure tensor which can be split up in the scalar pressure p_α and the anisotropic part $\mathbf{\Pi}_\alpha$, so that $\mathbf{P}_\alpha = p_\alpha \cdot \mathbf{I} + \mathbf{\Pi}_\alpha$. The scalar pressure relates to the temperature via $p_\alpha = n_\alpha T_\alpha$ and the anisotropic part depends on collisions and velocity gradients and describes the viscosity of the plasma. $\mathbf{q}_\alpha$ is the heat flow and $Q_{\alpha\beta}$ is the heat transferred from species α to species β by means of collisions. Each of the momentum equations represent a conservation law. Equation 1.10 is called the continuity equation. Equation 1.11 is referred to as the momentum balance and equation 1.12 is the equation of energy conservation. To determine the space-time evolution of n_α, $\mathbf{v}_\alpha$ and T_α by solving the fluid equations a description for $\mathbf{q}_\alpha$ in terms of the macroscopic quantities is required to provide closure for the equations.

1.3 Organization of the thesis

In this manuscript results obtained with the full-f gyrokinetic Elmfire code for the small Russian FT-2 tokamak are presented. The Introduction will be used to present the main highlights of the work. Furthermore the introduction will include details which have been left out from the publications but which provide valuable background information on how the final published results have been obtained. Chapter 2 will start by presenting the equations solved in the Elmfire code which are based on a set of gyrokinetic Vlasov equations which explicitly includes the polarization drift in the equations of motion by using an alternative definition for the gyrocenter. The differences to the standard gyrokinetic model and the advantages of this treatment for particle-in-cell codes are addressed. Publication V comments on a misunderstanding regarding the validity of this model. The dependence of the transport quantities of both the interpolation schemes, presented in publication VI, as well as the spatial resolution and particle noise are discussed and illustrated. The binary collision model is shortly addressed and a benchmark of the plasma resistivity to the Sauter model is presented. Direct measurements of transport phenomena in ohmic FT-2 discharges are shown to be quantitatively reproduced by the Elmfire simulation predictions in chapter 3. A detailed agreement with mean equilibrium $E \times B$ flows, oscillating fine-scale zonal flows and turbulence spectra observed by a set of sophisticated microwave back-scattering techniques as well as a good fit of the thermal diffusivity data are demonstrated in this publication. The measured and simulated mean equilibrium $E \times B$ flows are validated against various analytical models where the effect of the T_e/T_i-ratio, ion orbit losses and impurities are investigated in more detail providing a more solid basis for the findings on the background flow presented in publication VII. Linear growth rate results obtained with the Weiland reactive fluid model are presented to support the Elmfire results for the phase velocity presented in publication II, III, IV and VII.

2. The full-f particle-in-cell code Elmfire

The Elmfire code is based on the gyrokinetic Particle-In-Cell (PIC) method which follows the trajectories of charged particles in a self-consistent electrostic field computed on a fixed simulation grid. The Elmfire code calculates the full gyrokinetic distribution function (full-f) at every timestep making the code suitable to simulate turbulent and neoclassical transport, making it a powerful tool to simultaneously study both macro(background flow), meso (flow oscillation) and micro (turbulence) scale transport phenomena. In this section only a brief overview of the properties of the code that played an important role in the simulations of the FT-2 tokamak ohmic discharges are presented. A more complete overview of the code can be found in [17].

2.1 The Elmfire flowchart

The code starts by initializing the full-f gyrokinetic distribution function for ions and electrons according to the input profiles by introducing a large number of test particles equally spaced in configuration space and Maxwellian distributed in 2D velocity space onto the simulation grid. Each test particle will represent a large number of real particles. In the FT-2 tokamak simulations kinetic electrons and ions as well as one kinetic impurity species are taken into account. Since there is a significant difference between the impurity and the ion density the real-to-test-particle-ratio (from now on called weight ratio) of the impurities is taken to be 1/(charge of the impurity) times smaller than the weight ratio of the hydrogen isotopes and the electrons, to obtain similar particle statistics. To avoid strong deviations from the input profiles and the creation of strong start-up currents, the ions and impurities are initialized on pre-evaluated collisionless orbits while taking an appropriate analytical estimate for the radial electric field into account. To ensure quasi-neutrality at the start, an electron is initialized on the gyro-orbit of each ion and impurity.

After initialization, particles are moved by a Runge-Kutta particle pusher used for the integration of the explicit terms of the equations of gyrocenter motion. Heat sources and sinks are taken into account in the same particle loop as the particle pushing. The Elmfire code utilizes an implicit solver for the ion polarization drift and the electron parallel acceleration and the corresponding particle contribution of the implicit terms to the potential have to be collected in the coefficient matrix to solve the Poisson equation. For efficiency reasons this sampling is also performed in the same particle loop as the particle pushing. Once the particle pushing and collection of the implicit terms to the coefficient matrix is performed the charge separation is sampled to the grid and the potential is solved on the grid points. To obtain a quasi neutral system the particles still have to be moved by the implicit terms of the equations of gyrocenter, e.g. the polarization drift and the electron parallel acceleration, while taking the newly calculated potential into account. When the quasi neutral system is obtained, particles are allowed to collide by the binary collision model randomizing the particle velocity and pitch angle while leaving the particle positions untouched. After sampling the final macroscopic quantities to the grid the process is repeated until convergence of the system is reached. A schematic overview of the code's flowchart is given in figure 2.1.

In the following sections the separate parts of the Elmfire flowchart are outlined in more detail starting with the first two sections where the gyro center equations of motion and the corresponding electric field solver are presented. Section 4 outlines the different coordinate systems and the magnetic field background used in the ohmic FT-2 simulations followed by section 5 which shortly describes the binary collision operator. Section 6 will outline the different heating and cooling methods and the particle recycling schemes. The noise sensivity of the numerical model is discussed in the final section.

2.2 The equations of gyrocenter motion

During the last decades the nonlinear gyrokinetic approach has been widely used for numerical investigations into tokamak micro turbulence. As mentioned in the Introduction charged particles in a magnetic field will gyrate around the magnetic field lines. The gyrokinetic approach eliminates the explicit dependence of the Vlasov equations on the phase angle of the gyration by gyrophase-averaging while taking the electromagnetic perturbations of the field into account. This makes it unnecessary to solve for the fast time scale associated with the particle gyromotion while still retaining finite Larmor ra-

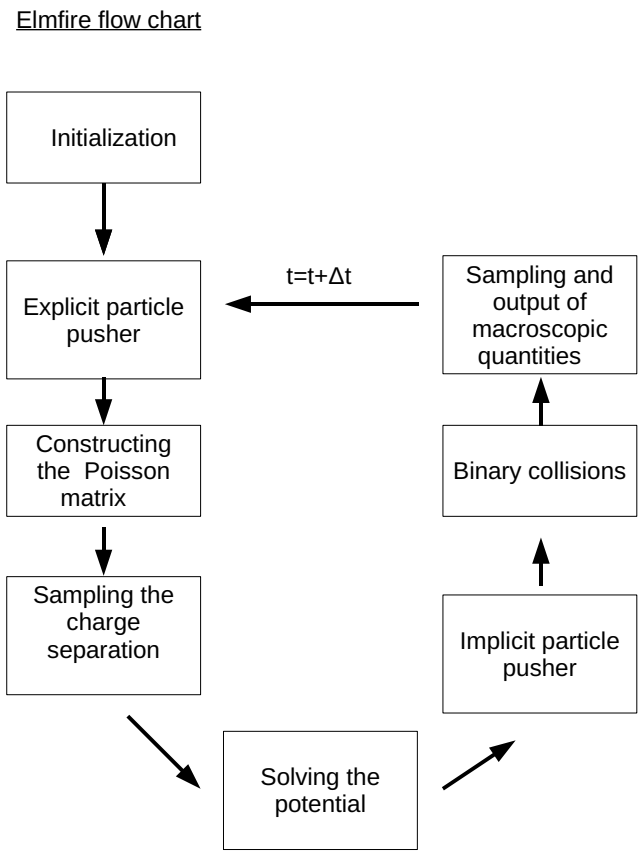

Figure 2.1. The flowchart of the Elmfire code

dius effects. The approach is only valid for fluctuations that remain within the nonlinear gyrokinetic ordering. This ordering requires that the perturbation frequencies ω are small compared to the ion cyclotron frequency of the gyromotion $\Omega_i = q_i B/m_i$ and the ion Larmor radius $\rho_i = v_{th,i}/\Omega_i = \sqrt{2T_i/(m_i\Omega_i^2)}$ small compared to the characteristic background scale length L. The scale length of the parallel perturbations are taken to be of the same order as the characteristic background scale length:

$$\frac{\omega}{\Omega_i} \sim \frac{\rho_i}{L} \sim \delta \qquad\qquad k_\parallel L \sim 1 \tag{2.1}$$

where $\delta \ll 1$ is the small ordering parameter. The equations solved in the Elmfire code are based on a set of gyrokinetic Vlasov equations which explicitly includes the polarization drift in the equations of motion by using the alternative definition for the gyrocenter $\mathbf{R} = \mathbf{x} - \mathbf{b} \times (\mathbf{v}_\perp - \mathbf{u}_E)/\Omega$ while gyrophase-averaging. Here $\mathbf{v}_\perp$ is the velocity vector perpendicular to the magnetic field unit vector $\mathbf{b} = \mathbf{B}/B$ and $\mathbf{u}_E = (\mathbf{b} \times \nabla\langle\phi\rangle_g)/B$ with $\langle\phi\rangle_g$ the gyroaveraged electrostatic potential. This alternative set of gyrokinetic equations was first derived by Sosenko *et al.* [19] and later on by Parra *et al.* [20] and Heikkinen *et al.* [21] while using Krylov-Bogoliubov averaging and by Wang *at al.* [22] while using the Lie-transform perturbation method. The full extent of the model, including the possibility of the model to be solved up to very high order in perturbation theory by including trembling terms of the gyrokinetic Poisson equation via Larmor radius correction, is demonstrated by Heikkinen *et al.* [21]. In the work presented in this thesis however we have restricted the model to be solved up to second order while neglecting second order nonlinear terms in the potential. As such we can adapt to the formulation presented by Heikinnen *at al.* where the equations of motion in terms of the gyrocenter position $\mathbf{R}$, the parallel gyrocenter velocity U and the gyrocenter magnetic moment μ are given by:

$$\begin{aligned}
\frac{d\mathbf{R}}{dt} &= U\mathbf{b} + \frac{1}{B^*}\mathbf{b} \times \left[\frac{\mu}{q_\alpha}\nabla B + \frac{m_\alpha v_\parallel^2}{q_\alpha}\mathbf{b}\cdot\nabla\mathbf{b} + \nabla\langle\phi\rangle_g\right] \\
&\quad - \frac{1}{\Omega B}\frac{\mathrm{d}\nabla\langle\phi\rangle_g}{\mathrm{d}t} \\
m\frac{dU}{dt} &= -\left(\mathbf{b} + \frac{m_\alpha v_\parallel}{q_\alpha B^*}\mathbf{b}\times\mathbf{b}\cdot\nabla\mathbf{b}\right)\cdot(\mu\nabla B + q_\alpha\nabla\langle\phi\rangle_g)
\end{aligned} \tag{2.2}$$

with

$$\mathbf{B}^* = B^*\mathbf{b} + \frac{m_\alpha v_\parallel}{q_\alpha}\mathbf{b}\times\mathbf{b}\cdot\nabla\mathbf{b} \tag{2.3}$$

$$B^* = B + \frac{m_\alpha v_\parallel}{q_\alpha}\mathbf{b}\cdot\nabla\times\mathbf{b} \tag{2.4}$$

These equations of motion include the $E\times B$-drift, the gradient and curvature drift as well as the polarization drift. Including the polarization drift explicit into the equations of motion does not change significantly the energy invariance of the system and as such the exact energy conservation law of the standard gyrokinetic model holds, as proven by Wang *et al.* [22]. The influence of the alternative definition of the gyrocenter on the Poisson equation and its advantage for PIC codes are discussed in the next section. The electrons are treated drift kinetically by setting the Larmor radius to zero.

2.3 Electric field calculation

2.3.1 The Poisson equation

The radial electric field evolution in a gyrokinetic code is obtained by solving the quasi neutral gyrokinetic Poisson equation for the ensemble average of the gyrocenter motions. The Poisson equation for the real particle densities n_α is given by:

$$\nabla^2\phi = -\frac{\sum_\alpha q_\alpha n_\alpha}{\varepsilon_0} \tag{2.5}$$

where α runs over all particle species. This formula illustrates that when non ambipolar particle motion cause a charge separation in a plasma a radial electric field is created. The polarization drift $v_p = -(m/q_\alpha B^2)d\nabla_\perp\phi/dt$ restores quasi neutrality by generating the polarization density which counter balances the charge density created by the non ambipolar particle flux. The real particle density is related to the gyrocenter particle density by:

$$n_\alpha = \int F_I(\mathbf{R}, U, \mu, \theta)\delta^3(\mathbf{R} + \rho - \mathbf{x})|J|d^3RdUd\mu d\theta \tag{2.6}$$

where F_I is the standard gyrocenter distribution function and $|J|$ the Jacobian for the transformation from the particle phase space to the gyrocenter phase space. The distribution function solved for in PIC codes, also referred to as the primary form of the distribution function, automatically takes the changes in gyrocenter phase space volume into account while sampling the "pushed" particles to the grid and is related to the standard gyrocenter distribution function as:

$$F_p(\mathbf{R}, U, \mu, \theta)d^3RdUd\mu d\theta = F_I(\mathbf{R}, U, \mu, \theta)|J|d^3RdUd\mu d\theta \tag{2.7}$$

The long wavelength limit ($k_\perp L \sim 1$) polarization density for the ions in terms of the gyrocenter variables is given by:

$$n_{\alpha,pol} = \frac{q_\alpha^2}{m_\alpha B \varepsilon_0} \int d^3R dU d\mu d\theta (\phi - \langle\phi\rangle_g) \frac{\delta F_p}{\delta \mu} \delta^3(\mathbf{R} + \rho - \mathbf{x}) \tag{2.8}$$

To sample $\frac{\delta F_p}{\delta \mu}$ with a full-f PIC method is impossible and an analytical approximation calculated from a Maxwellian distribution is often used to solve the Poisson equation. When the polarization drift is explicitly included in the gyrocenter equations of motion by defining the gyrocenter variable as $\mathbf{R} = \mathbf{x} - \mathbf{b} \times (\mathbf{v}_\perp - \mathbf{u}_E)$ the long wavelength limit of the polarization density will vanish and the Poisson equation for a pure plasma will reduce to the simple form:

$$\nabla^2 \phi(\mathbf{x}, t) = -\frac{[q_i N_i(\mathbf{x}, t) + q_e n_e(\mathbf{x}, t)]}{\varepsilon_0} \tag{2.9}$$

where N_i is now expressed in terms of the primary distribution function F_p as defined in publication V. It was the different definition of the particle distribution function which lead to a misunderstanding concerning the validity of the gyrokinetic model used in the Elmfire code. All controversies have, however, been resolved in publication V and [24]. By defining the gyrocenter variable as $\mathbf{R} = \mathbf{x} - \mathbf{b} \times (\mathbf{v}_\perp - \mathbf{U}_E)$ instead of the standard definition $\mathbf{R} = \mathbf{x} - \mathbf{b} \times \mathbf{v}_\perp$ no Maxwellian assumption for the distribution function is needed to solve the Poisson equation with the PIC method making the approach more consistently full-f.

2.3.2 The implicit Poisson solver

The Elmfire code evaluates the potential implicitly by linearizing the density change in each grid point caused by the ion polarization drift and the electron parallel acceleration. Considering how the linearized densities change in time, the Poisson equation can be rewritten as:

$$\begin{aligned} 0 = N_i(x_j, t) - n_e(x_j, t) = N_i(x_j, t - \Delta t) \\ + \delta N_{i,w/o\ pol.drift}(x_j, \phi(x_{j1,\ldots,j_m}, t - \Delta t)) \\ + \delta N_{i,pol.drift}(x_j, \phi(x_{i_1,\ldots,i_n}, t) - \phi(x_{j1,\ldots,j_m}, t - \Delta t)) \\ - n_e(x_j, t - \Delta t) - \delta n_{e,w/o\ par.accel.}(x_j, \phi(x_{j1,\ldots,j_m}, t - \Delta t)) \\ - \delta n_{e,par.accel.}(x_{i1,\ldots,i_n}, \phi(x_j, t)) \end{aligned} \tag{2.10}$$

The contribution of the density change to the potential has to be sampled to a matrix to solve for the potential and is calculated particle wise. Depending on

the field interpolation scheme, described in the next section, each contribution of every particle affects the potential in several surrounding grid cells $(i_1, ..., i_n)$ and $(j_1, ..., j_m)$. The field interpolation stencil has to be chosen so that the matrix is well posed to prevent problems with the matrix inversion. Neumann and/or Dirichlet boundary conditions for the potential are used at the inner and outer radial simulation boundary. To obtain stable boundaries flux surface averaging of the charge separation is performed in a buffer region near the boundaries.

2.3.3 Electric field interpolation scheme

While particles can be located anywhere in the simulation domain, the macro quantities are calculated on the simulation grid-points by sampling the test particles to the grid according to a test particle shape function $S_k(x)$. The electrons are sampled at the guiding center position. For the ions four points are chosen on the ion Larmor radius and at each of those points sampling is performed with one quarter of the ion weight ratio. The Elmfire code utilizes the cloud-in-cell shape function for sampling the particles, which is a simple first order linear weighting scheme. After sampling the charge separation to the grid the potential is implicitly solved on the same grid as used for the particle sampling. When the particles are moved the local electric field for every particle position is recovered from the grid via a field weighting interpolation scheme, which describes the weighting of the potential of the surrounding grid-cells to the local particle position. The Elmfire code has two different field weighting schemes implemented. Scheme I uses the same weighting scheme for the particles and the electric field:

$$\mathbf{E}(\mathbf{x}) = \sum E_k S_k(\mathbf{x} - \mathbf{x}_k) \tag{2.11}$$

Scheme II uses the same weighting scheme for the particles and the potential, making the electric field a function of the gradient of the particle weighting scheme:

$$\mathbf{E}(\mathbf{x}) = -\nabla\phi = -\sum \phi_k \nabla S_k(\mathbf{x} - \mathbf{x}_k) \tag{2.12}$$

Scheme II is numerically stable against divergent $E \times B$ flow, as proven by Byers *et al.* [25], but does not conserve toroidal angular momentum leading to a self-force acting on the particles. As a result a nonambipolar $E \times B$ radial current is produced. Scheme I conserves toroidal angular momentum and therefore keeps the $E \times B$ flow ambipolar. Unfortunately this scheme is prone to numerical instability by divergent $E \times B$ flow. In publication VI a modification to scheme I is presented which forces the toroidal component of

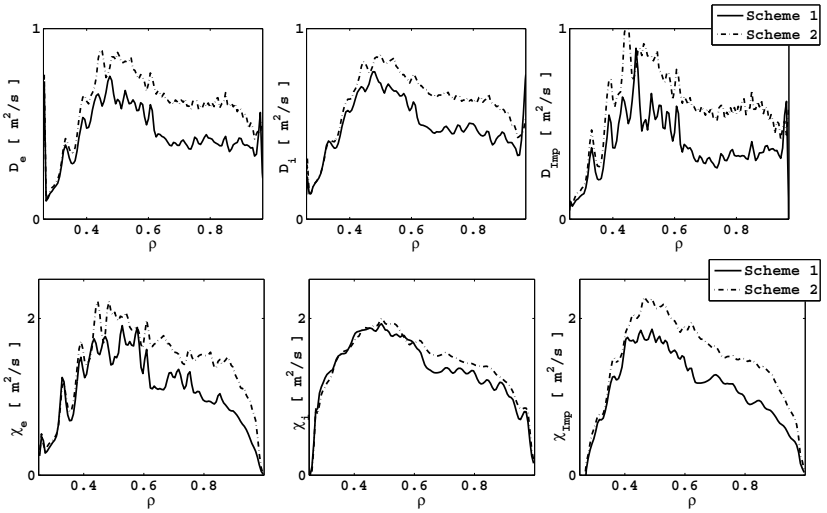

Figure 2.2. The particle diffusion coefficients (top) and the heat conductivity (down) for the electrons, ions and impurities averaged over 60 μs for the turbulent stage while using Scheme I and scheme II for the field interpolation. The simulation parameters are presented in publication VII.

the curl of E to be zero, stabilizing the scheme. The influence of the field weighting schemes on the particle transport is illustrated in figure 2.2 showing the diffusion and heat coefficients for the simulation parameters presented in publication VII. A simulation grid of 120x150x8 in radial/poloidal/toroidal direction was used for both simulations. A clear increase of the transport coefficients is seen when scheme 1 is used. The toroidal angular momentum conservation for the two schemes is presented in figure 6 of Publication VI. The flux-surface-averaged radial electric field averaged over 60 μs of the saturated turbulent state and its envelope are presented in figure 2.3 and 2.4. The burstiness of the radial electric field in scheme I is increased compared to scheme II and the average radial electric field is more negative. In publications I and II scheme II for the field interpolation was used. The simulations presented in the other publications and in the Introduction part of this manuscript use interpolation scheme I.

2.4 Magnetic field background, coordinate systems and spatial resolution

The Elmfire simulation results presented in this work have utilized an analytical circular quasi-toroidal magnetic field equilibrium expressed by

$$\mathbf{B} = \frac{R_0}{R}\left(B_p(r)\mathbf{e}_\theta + B_t\mathbf{e}_\phi\right) = B_\theta\mathbf{e}_\theta + B_\phi\mathbf{e}_\phi \tag{2.13}$$

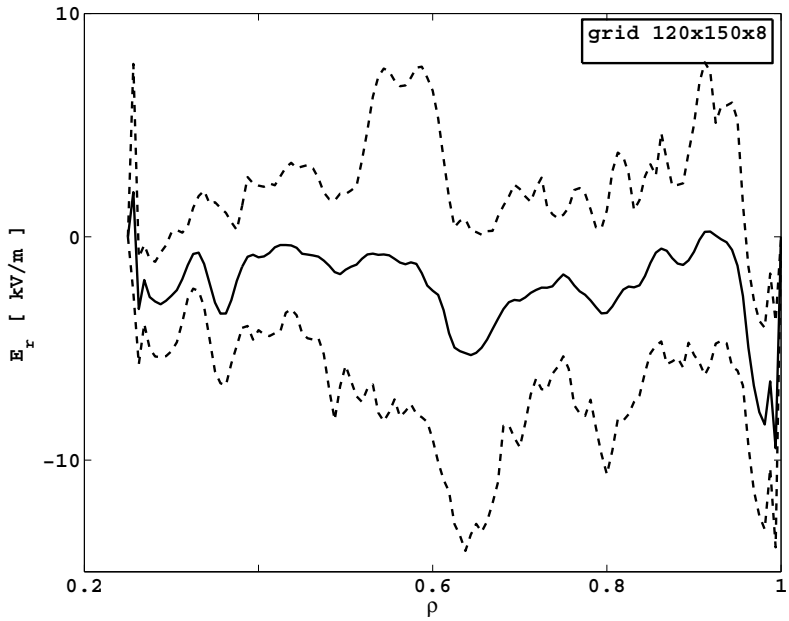

Figure 2.3. The flux-surface-averaged radial electric field averaged over 60 μs (-) and its envelope (--) obtained with interpolation scheme I for the simulation parameters presented in publication VII

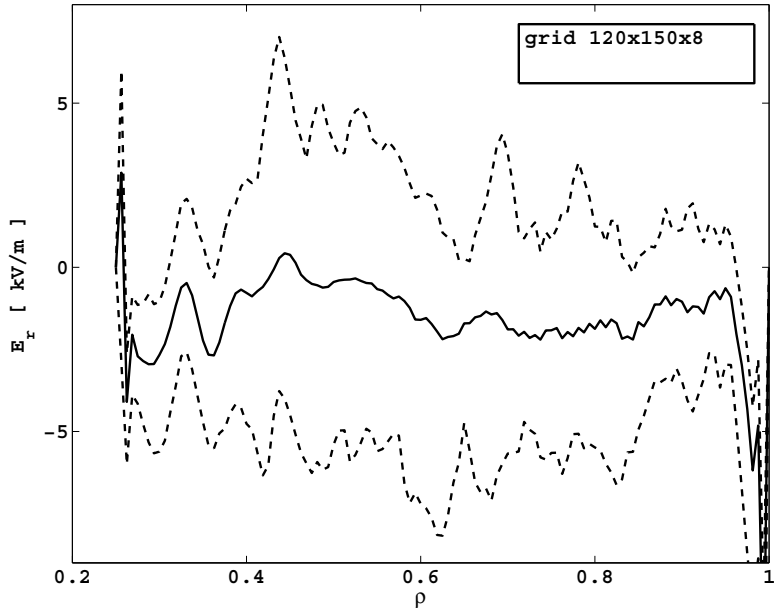

Figure 2.4. The flux-surface-averaged radial electric field averaged over 60 μs (-) and its envelope (--) obtained with interpolation scheme II for the simulation parameters presented in publication VII

where B_t is the on axis toroidal magnetic field, $R = R_0 + r\cos\theta$ the radial distance from the symmetry axis of the tokamak, R_0 the major radius of the tokamak and $r/\theta/\phi$ the radial/poloidal/toroidal coordinate. B_p is the flux-surface-averaged poloidal magnetic field and its radial dependence is given by:

$$B_p(r) = \sqrt{1-\epsilon^2}\frac{\mu_0 I(r)}{r} \tag{2.14}$$

with $\epsilon = r/R_0$ the inverse aspect ratio and $I(r)$ the radial plasma current defined as:

$$I(r) = \frac{I_0}{2\pi}\left[1 - \left(1 - \frac{r^2}{a^2}\right)^{\alpha_j+1}\right] \tag{2.15}$$

I_0 is the total plasma current and a the minor radius of the tokamak. To minimize computational expenditure while obtaining enough accuracy two different coordinate systems are used in the code. Orbits are followed in straight-field line coordinates (r, θ_w, ζ) [26] while the grid used for sampling and solving the potential utilizes quasi-ballooning coordinates (r, χ, ζ) [27]. The choice of coordinates of the grid is made to set the toroidal-poloidal periodicity by introducing a misalignment to the magnetic field via exact offset-periodic meshing of the grid lines at the boundary. The coordinate transformation from the straight field line coordinates to the quasi-ballooning coordinates is given by:

$$\chi = \theta_w - \frac{1}{q(r)}\zeta \tag{2.16}$$

where $q(r)$ is the safety factor. Equidistant spacing for the grid cells is used in all three quasi-ballooning coordinates resulting in larger grid cells on the outboard side of the torus compared to the inboard side when transformed to toroidal coordinates.

To obtain a correct nonlinear saturated state of turbulence, the radial resolution has to be high enough so that the magnetic shear $\mathbf{s} = r\Delta q/(q\Delta r)$ can be accurately reproduced. When this is not the case the turbulent streamers will not be correctly sheared leading to an overestimate of the radial transport. For large toroidal mode numbers the rational surface spacing is estimated by $\Delta q \approx (m+1)/n - m/n = 1/n$, where m and n are the poloidal and toroidal mode number, respectively. Substituting the rational surface spacing into the magnetic shear equation we find that the required radial spacing has to be $\Delta r = r/(m\mathbf{s})$ [28]. The minimum required radial resolution is found by taking m to be equal to the number of poloidal grid cells (= highest possible m number). In figure 2.5 the diffusion and heat conductivity coefficients are shown for a low radial resolution simulation and a high radial resolution simulation. The low radial resolution simulation has grid size 30x200x8 in radial/poloidal/toroidal direction and does not fulfill the minimum radial surface

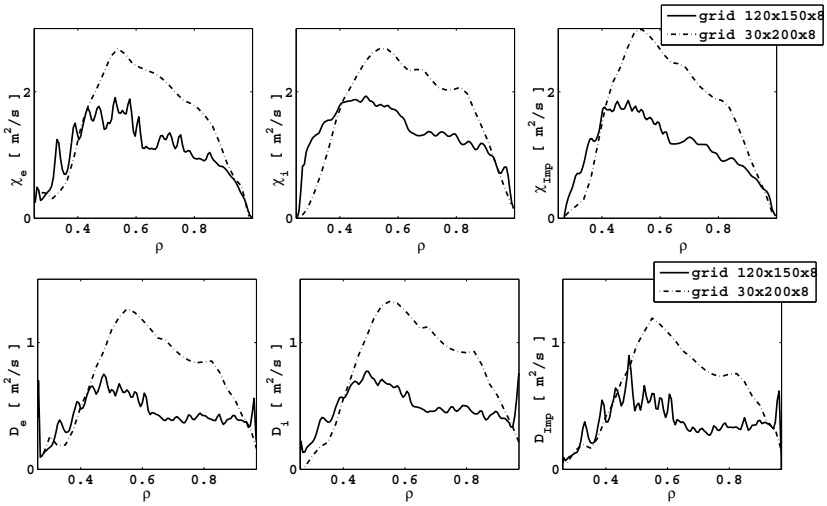

Figure 2.5. The particle diffusion coefficients (top) and the heat conductivity (down) for the electrons, ions and impurities averaged over 60 μs for the turbulent stage while using grid size 30x200x8 (--) and grid size 120x150x8 (-) in radial/poloidal/toroidal direction for the simulation parameters presented in publication VII.

spacing while the high radial resolution simulation has grid size 120x150x8 which does fulfill the radial resolution requirement. Much higher transport coefficients are found for the radially under resolved simulation. The flux-surface-averaged radial electric field averaged over 60 μs (-) and its envelope (--) for the saturated turbulent state is presented in figure 2.6 and 2.7. A difference in both the average as well as the burstiness of the radial electric field is seen between the two resolution cases.

2.5 The binary collision model

In order to establish a correct long time statistical equilibrium of the total particle distribution function an accurate collision operator is required for both pitch angle scattering and energy diffusion and slowing down. Although the collisional transport in tokamaks is expected to be much smaller than the turbulence induced transport, the collisional transport does become important in the case when turbulent transport is significantly reduced, like in the L-H transition. On top of that the collision operator performs the important task of returning distorted distributions back to the Maxwellian distribution. Calculating the equilibrium distribution function for a collisional gyrokinetic system is nontrivial and only in a very few cases when drastic assumptions are allowed an analytical result can be obtained. The most important criterion for

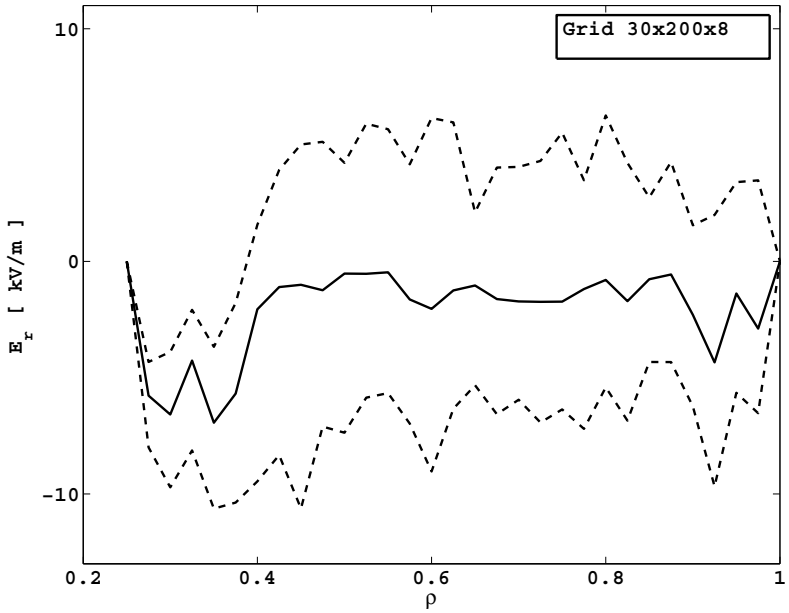

Figure 2.6. The flux-surface-averaged radial electric field averaged over 60 μs (−) and its envelope (--) as a function of normalized radius for grid size 30x200x8 for the simulation parameters presented in publication VII.

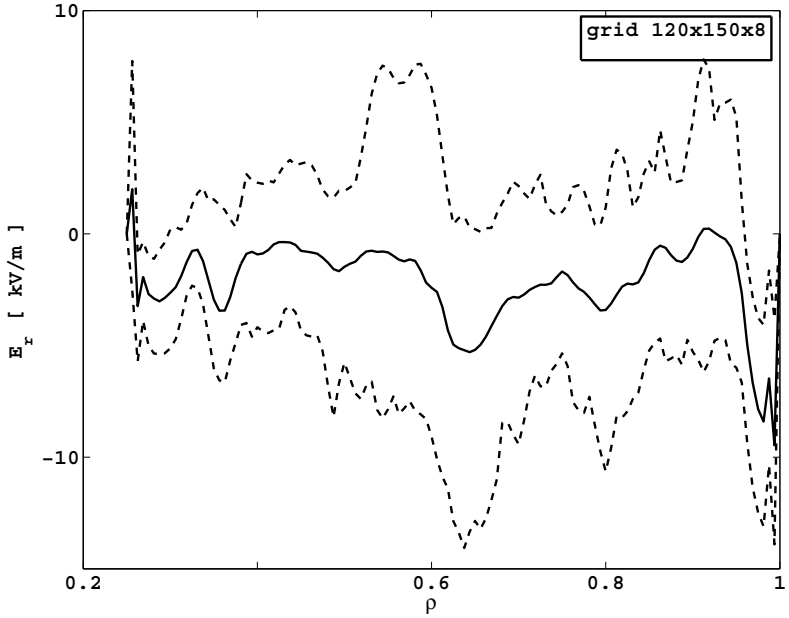

Figure 2.7. The flux-surface-averaged radial electric field averaged over 60 μs (−) and its envelope (--) as a function of normalized radius for grid size 120x150x8 for the simulation parameters presented in publication VII.

a collision operator in a full-f gyrokinetic code is to conserve particles, energy and momentum both locally and globally as otherwise artificial plasma flows can easily be created.

The Elmfire code utilizes the binary collision model which treats collisions by applying a pairwise collision operator to the test particles. It is clear that it would be an impossible task to calculate binary collisions accurately on a particle-to-particle basis for the complete particle distribution. But since we are interested in simulating the macroscopic net effect of the binary collisions to the entire system a Monte Carlo type operator can be used. The Elmfire code has adopted the binary collision model as first presented by Takizuka *et al.*[29]. This model starts by grouping test particles that reside within a similar plasma background after which these particles are randomly paired and let to collide like if they were regular physical particles. While colliding the two test particles the relative velocity $\mathbf{u_r}$ of the two particles is altered by a scattering angle. The scattering is chosen randomly from a Gaussian distribution with mean zero and a variance determined by the angular relaxation rate $\nu_{\alpha\beta}$ multiplied with the timestep. For a collision between species α and species β $\nu_{\alpha\beta}$ is given by:

$$\nu_{\alpha\beta} = \frac{q_\alpha^2 q_\beta^2 n_\beta \lambda_{\alpha\beta}}{8\pi\epsilon_0^2 m_{\alpha\beta}^2 |u_r|^3} \tag{2.17}$$

where $m_{\alpha\beta} = m_\alpha m_\beta/(m_\alpha + m_\beta)$ and $\lambda_{\alpha\beta}$ is the coulomb logarithm defined for electron-electron collisions as:

$$\lambda_{ee} = 23.5 - \ln(n_e^{1/2} T_e^{-5/4}) - [10^{-5} + (\ln T_e - 2)^2/16]^{1/2} \tag{2.18}$$

for electron-ion collisions:

$$\begin{aligned}
\lambda_{ei} &= 23 - \ln(n_e^{1/2} Z T_e^{-3/2}), \qquad T_i m_e/m_i < T_e < 10Z^2 eV & (2.19)\\
&= 24 - \ln(n_e^{1/2} T_e^{-1}), \qquad T_i m_e/m_i < 10Z^2 eV < T_e & (2.20)\\
&= 30 - \ln(n_i^{1/2} T_i^{-3/2} Z^2 \mu^{-1}), \qquad T_e < T_i Z m_e/m_i & (2.21)
\end{aligned}$$

and for mixed ion-ion collisions as:

$$\lambda_{ii'} = 23 - \ln\left[\frac{ZZ'(\mu+\mu')}{\mu T_{i'} + \mu' T_i}\left(\frac{n_i Z^2}{T_i} + \frac{n_{i'} Z'^2}{T_{i'}}\right)^{1/2}\right] \tag{2.22}$$

where μ is the ion mass normalized to the proton mass, Z is the ion charge state. In equation 2.18-2.22 the density $n_{e/i}$ and temperature $T_{e/i}$ are in units of [cm^{-3}] and [keV], respectively. The length of the relative velocity vector is left untouched leaving the energy conserved. The new velocities of the two colliding test particles are calculated from the new relative velocity while

making sure that the momentum remains conserved. During the time interval Δt every particle has collided at least once with every particle species. As long as the time interval is chosen sufficiently small compared to the relaxation time of the system the collision model nicely reproduces the theoretical estimates of the slowing-down rate, the energy transfer rate, the deflection rate and the energy exchange rate obtained with the Landau collisional integral, as shown in [29]. On top of a very short time step, the collisional grid should be small enough in the radial direction and sufficient particles per collision grid cell are required for accurate statistics. Gyrokinetic corrections are omitted in this collision model.

2.6 Sources and Sinks

Full-f gyrokinetic codes solve for both the plasma perturbations as well as the plasma background. As a result the background profiles are able to evolve in time and will change due to radial particle and heat transport. Only when there are accurate sources and sinks included in the simulation a long time saturated equilibrium state close to the experimentally measured profiles can be reached. In this section the heat and particle sources and sinks used in publication VII are presented.

2.6.1 Ohmic heating

Toroidal current, created by applying a loop voltage to the plasma and needed to achieve the magnetic equilibrium in a tokamak, is also a source of plasma heating. When a loop voltage is applied to a plasma the electrons are accelerated until the acceleration force is balanced by the ion-electron collision force creating a large steady state electron flow velocity. The plasma resistivity scales with $T_e^{-3/2}$ making ohmic heating a rather weak energy source for larger fusion experiments where the electron temperature is in the keV range. For the small FT-2 tokamak however the electron temperature remains within several 100 eV making ohmic heating a rather effective heating source. In the simulations presented in publication VII ohmic heating is simulated by applying a radially uniform loop voltage ramping up and sustaining the prescribed total plasma current of 18.9 kA. Figure 2.8 shows the time evolution of the electron parallel flow $v_{\parallel,e}$ for this simulation where a saturated state is found after an initialization period of 5 μs. The efficiency of a loop voltage as a heating source is depending on the parallel conductivity and can be obtained

from Elmfire simulations by Ohm's law:

$$\sigma_{\parallel} = \frac{\langle j_{\parallel} \rangle}{\langle E_{\parallel} \rangle} = \frac{q_e \langle n_e \rangle \langle v_{\parallel,e} \rangle - \langle j_{b,e} \rangle}{\langle E_{\parallel} \rangle} \tag{2.23}$$

where $\langle .. \rangle$ denotes the flux-surface-average, $j_{\parallel}$ the parallel current and j_b the bootstrap current. The analytical estimate for the classical conductivity is given by the Spitzer conductivity [30]:

$$\sigma_{Sptz} = 1.9012 \cdot 10^4 N\left(Z_{eff}\right) \frac{T_e^{3/2}}{31.3 - \ln(\sqrt{n_e}/T_e])} \tag{2.24}$$

where $N(Z_{eff})$ accounts for the impurity contribution:

$$N(Z_{eff}) = \frac{0.76 + Z_{eff}}{Z_{eff}(1.18 + 0.58 Z_{eff})} \tag{2.25}$$

where the effective charge $Z_{eff} = \sum_j n_j Z_j^2 / \sum_j n_j Z_j$ with Z_j the ion charge state and j running over all ion species. To obtain an expression for the neoclassical conductivity the contribution of the trapped particles has to be accounted for as well as the detrapping effect of a toroidal electric field [35, 36]. The most commonly used expression for the parallel neoclassical conductivity σ_{NC} has been obtained with numerical simulations presented by Sauter *et al.* [37] where the Fokker-Planck equation with the full collision operator for a wide variety of plasma and equilibrium parameters were solved:

$$\frac{\sigma_{NC}}{\sigma_{Sptz}} = 1 - \left(1 + \frac{0.36}{Z_{eff}}\right) X + \frac{0.59}{Z_{eff}} X^2 - \frac{0.23}{Z_{eff}} X^3 \tag{2.26}$$

with

$$X = \frac{f_t}{1 + (0.55 - 0.1 f_t)\sqrt{\nu_{e*}} + 0.45(1 - f_t)\nu_{e*}/Z_{eff}^{3/2}} \tag{2.27}$$

where f_t is the trapped particle fraction as defined in section 1.1 and $\nu_{e*} = 6.921 \cdot 10^{-18} q_e R^{5/2} n_e Z_{eff}(31.3 - \ln(\sqrt{n_e}/T_e))/(T_e^2 r^{3/2})$. Figure 2.8 shows the parallel conductivity obtained with the Elmfire code calculated with equation 2.23 compared to the neoclassical conductivity obtained with the Sauter model for several values of Z_{eff}. A very good agreement is found for all Z_{eff} values. No substantial influence of the electrostatic turbulence to the parallel conductivity is found.

2.6.2 Particle losses and heat control

The Elmfire code does not solve for the magnetic axis and therefore the simulation domain has an inner and outer radial boundary. For particles passing the inner boundary the orbit trajectory of the particle is calculated (without

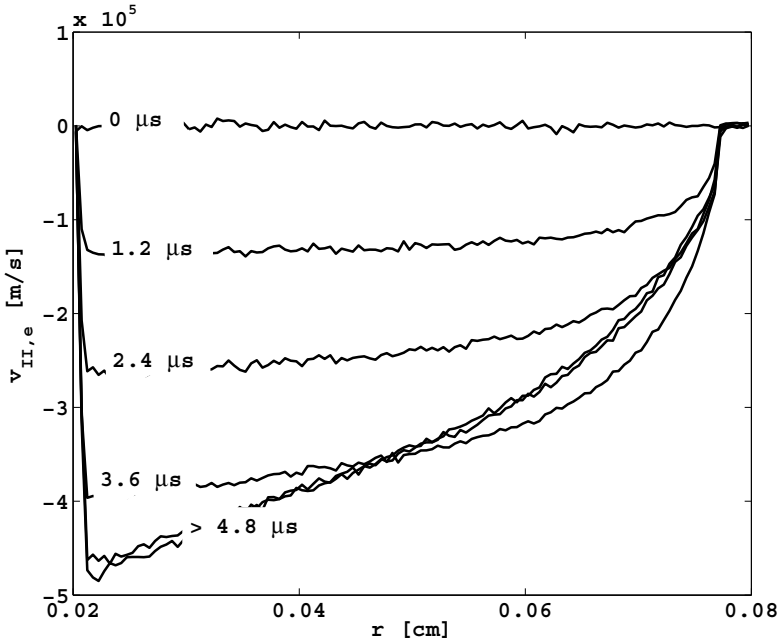

Figure 2.8. The flux-surface-averaged electron flow velocity parallel to the magnetic field as a function of radius for different time durations of the simulation.

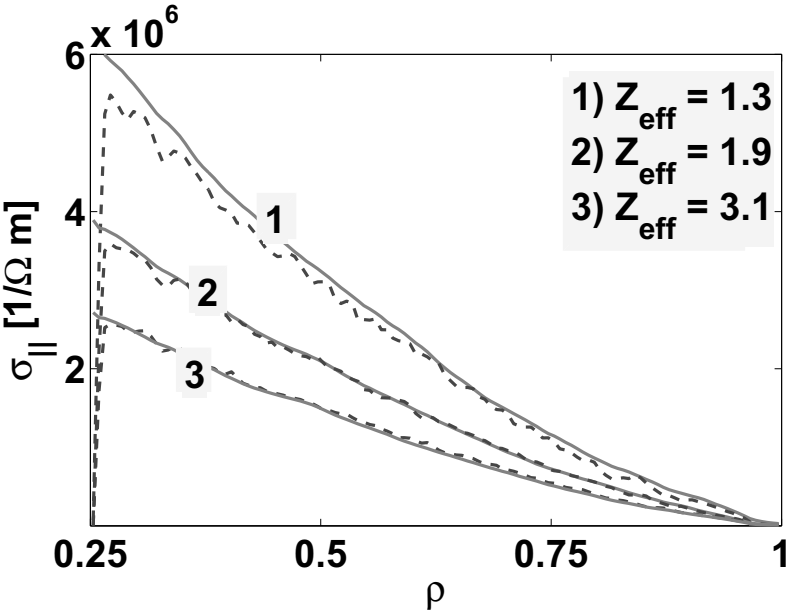

Figure 2.9. The parallel conductivity simulated by the Elmfire code (--) and the Sauter model (−) for Z_{eff} is 1.3, 1.9 and 3.1. Adopted from [38]

taking collisions into account) up to the position where the particle would re-enter into the simulation domain. Particles passing the outer boundary are reinitialized into the simulation domain as an electron-ion pair according to a prescribed profile. In publication VII the prescribed profile is based on the measured radial profile of the neutral hydrogen density in the FT-2 tokamak. When there is an unequal amount of electrons and ions flowing out, the remaining unpaired particles after neutral reinitialization are reinitialized near the outer boundary.

Due to the flux surface averaging of the charge separation near the boundaries, turbulence is suppressed in this area and particles are not flowing out fast enough from the outer simulation domain. As a result a particle accumulation near the outer boundary can be seen from the particle density. To increase the removal of particles near the outer boundary the particle outflow caused by the two FT-2 poloidal limiters is modeled by assigning a random toroidal distance, ranging between 0 and πR_0 (R_0=the major radius), to each ion entering the outer layer of the simulation domain shadowed by the limiters. When the ion has traveled the assigned distance it is recycled back into the plasma according to the same prescribed profile used for reinitialization. For every removed ion a random electron from the same radial position is simultaneously removed. The model successfully prevents particle accumulation near the outer boundary and captures the most prominent features of the recycling process. Since fast ions are removed faster than slow ions this model also provides cooling near the outer boundary. In publication VII the cooling of the electrons is performed according to the experimental fit of the power density of the impurity radiation and ionization given by $P_{rad} = 3.5 \times 10^6(-0.16\rho \exp(8\rho - 8) + 0.08\rho + 0.15)$ W/m^3 with $\rho = r/a$ the normalized radius.

When only a small region of the plasma configuration is simulated, as in publication VIII, the temperatures near the boundaries are controlled with a background collision model. The background collision model is based on a basic Monte Carlo energy diffusion collision operator where particles are allowed to collide with a Maxwellian background. When the background Maxwellian has a higher/lower temperature than the simulated plasma particles, the particles will be heated/cooled respectively. To make the collision model more effective as a heating/cooling source a higher collisionality than the one obtained from the Maxwellian background is often used.

2.7 Noise in the Elmfire particle-in-cell code

In the Elmfire code the electron, ion and impurity densities are obtained by sampling the test particles onto the simulation grid. Due to the finite test particle number the density fluctuations will not only include physics such as neoclassical effects and turbulence but also numerical effects arising from noise and initialization. In general it is assumed that the noise in particle-in-cell simulations reduces as $(\delta n/n)_{noise} \propto 1/\sqrt{N}$ where N is the average number of test particles in each cell. The Elmfire code applies the cloud-in-cell method, rather than the particle-in-cell method, which will bring down the noise level. The 4-point gyro-averaging method used for the particle sampling of ions will further reduce the noise level. An estimate for the fluctuation level for fully developed turbulence can be quantified by using the mixing-length estimate for the nonlinear saturation state of the turbulence $(\delta n/n)_{turbulence} \propto 1/(k_\perp L_n)$ where L_N is the density gradient scale length. Assuming that the most dominant turbulent fluctuations in the nonlinear turbulent stage will have $k_\perp \rho_i \approx 0.1 - 0.3$ and taking the density profile from the simulation presented in publication VII where $L_{N_i}/\rho_i <\sim 50 - 100$ an average turbulence fluctuation level of 5% is found indicating that as little as 500 particles per grid cell could be sufficient to recover turbulent fluctuations for the typical ohmic FT-2 plasma parameters. For larger tokamaks the density gradients in the core are normally weaker and $L_{N_i}/\rho_i \approx 500$ making these simulations more demanding, not just because of the larger size of the tokamak but also due to the lower turbulence fluctuation level. The fluctuation level for neoclassical fluctuations goes as $(\delta n/n)_{noise} \propto \epsilon \cos\theta$ [39] making the neoclassical effects much easier to recover than the turbulent effects.

The fluctuation level of density and fluxes caused by noise and initialization can be studied by analyzing the density fluctuation level at the start up of the simulation, when the neoclassical and turbulent effects have not yet developed. Figure 2.10 shows the ion density fluctuation level at the outboard side as a function of normalized radius averaged over the first 100 timesteps and a clear reduction of the noise fluctuation level is observed when increasing the test particle number. Figure 2.11 shows the noise fluctuation level presented in figure 2.10 averaged over the radial domain $\rho = 0.3 - 0.8$ together with the $1/\sqrt{N}$ value. From these results it can be clearly seen that when more than 3000 test particles per grid cell are used on average, the noise level will be smaller than 1%. Because the fluctuation level caused by the initialization also reduces when more test particles are initialized it is difficult to determine

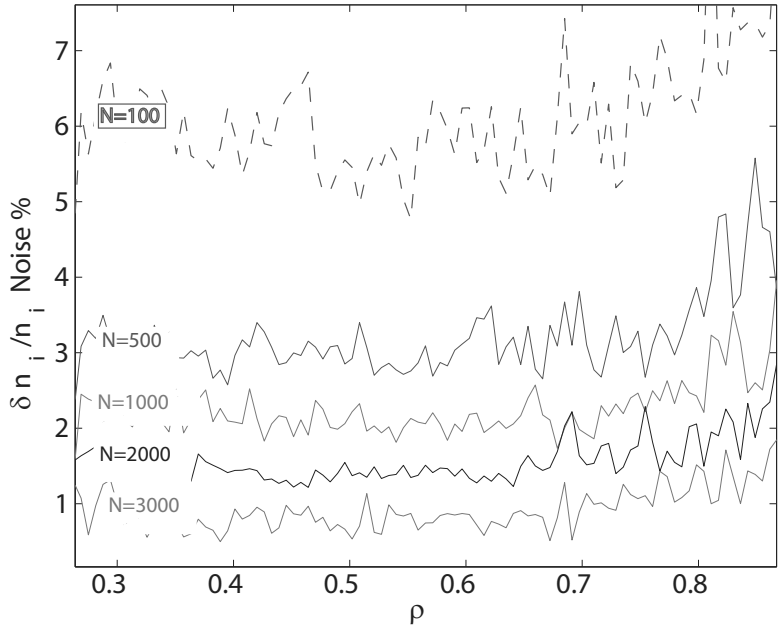

Figure 2.10. The noise level of the ion density fluctuations as a function of normalized radius for various number of average test particles per grid cell.

a dependence of just the particle noise on the number of test particles. In figure 2.12 the fluctuation level of the ion density in the turbulent saturated state for varying particles number is presented. From an average number of 500 particles per grid cell the turbulent fluctuation level is of the same order as the noise fluctuation level and when an average number of 3000 particles per gridcell are used the noise fluctuation level is clearly much lower than the turbulent fluctuation level and convergence of the simulation results to particle number is obtained.

In the presented simulations the particle weight ratio (= the amount of real particles represented by one test particle) is kept constant in time and as such noise accumulation, as is common in simulations with varying particle weight, will not occur in these simulations. When weak dissipation is present in the simulation, noise accumulation (weak occupation of some parts of phase space) can occur in the velocity space when turbulence develops. The simulations presented in publication VII are highly collisional (effective collisionality $\nu_* = 10 - 25$) and as such the level of dissipation is high enough to overcome this problem.

Figure 2.13 and 2.14 show the particle and heat flux as a function of time for two simulations with 100 and 3000 test particles per grid cell at normalized

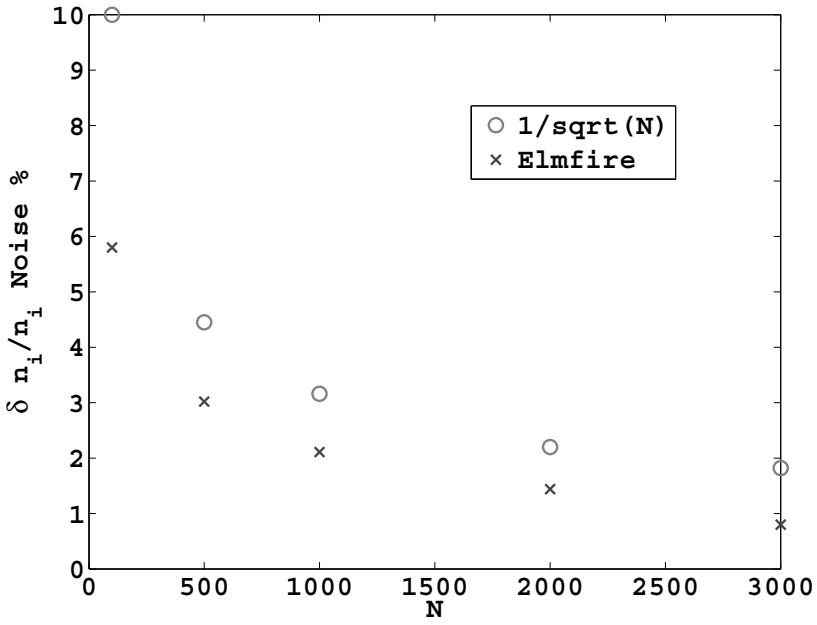

Figure 2.11. The noise level of the density fluctuations as a function of average test particle number per grid cell.

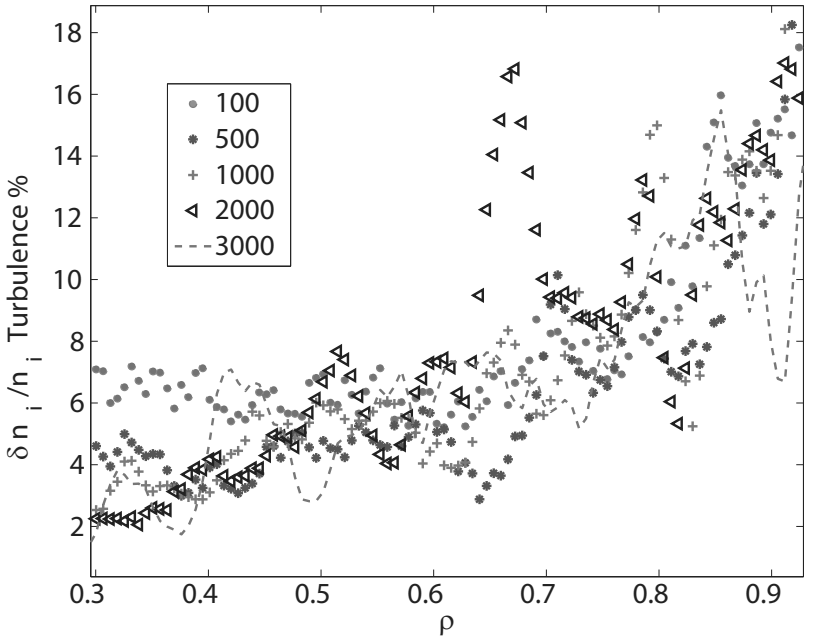

Figure 2.12. The turbulent ion density fluctuation level at the outboard side of the tokamak as a function of normalized radius for various number of average test particles per grid cell.

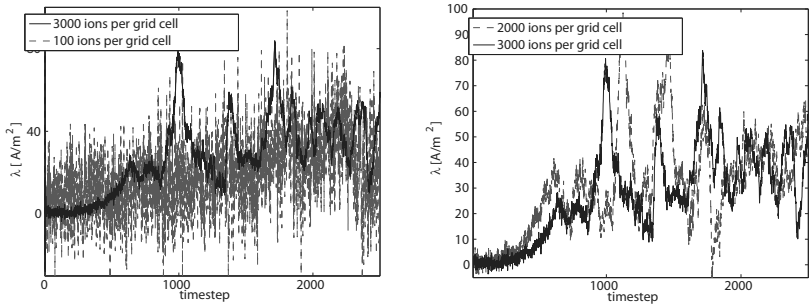

Figure 2.13. The particle flux as a function of timestep for the simulation parameters presented in publication VII while using 100 and 3000 test particles per grid cell on average (left) and while using 2000 and 3000 test particles per grid cell on average (right).

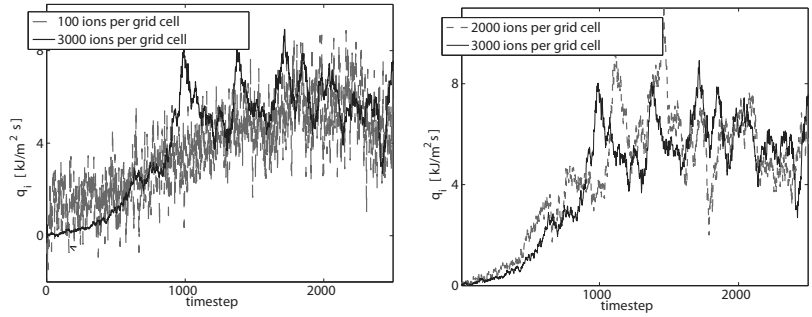

Figure 2.14. The heat flux as a function of timestep for the simulation parameters presented in publication VII while using 100 and 3000 test particles per grid cell on average (left) and while using 2000 and 3000 test particles per grid cell on average (right).

radius $\rho = 0.65$. It is interesting to notice that in figure 2.13a and 2.14a the average level of the fluxes is reasonably similar at the end state of the simulation but that the bursts observed in the 3000 test particle per grid cell simulation are not recovered in the 100 test particles per grid cell simulation. This indicates that the dominant neoclassical fluxes have been obtained in both cases. To prove that the bursts are fully converged with respect to the test particle number figures 2.13b and 2.14b present the heat and particle fluxes at $\rho = 0.65$ for the simulations with 2000 and 3000 particles per grid cell. Little difference is found between both the average fluxes as well as the dynamics of the fluxes between the two simulations.

3. Turbulence and plasma flows in ohmic FT-2 discharges

In this chapter direct measurements of micro, meso, and macro-scale transport phenomena in the FT-2 tokamak are compared to global full f nonlinear gyrokinetic simulation predictions by means of a synthetic Doppler reflectometry diagnostic. The effect of the impurity ratio, the T_e/T_i ratio and the ion orbit losses on the mean equilibrium $E \times B$ flow are clearly illustrated by a set of parameter scans performed with the Elmfire code. The growth rates and frequencies for the main turbulent instabilities present in ohmic FT-2 discharges are investigated and the turbulence driven E_r dynamics are examined.

3.1 A synthetic Doppler reflectometry diagnostics

Reflectometry is a radar technique which uses back scattered reflection of electromagnetic waves by a plasma cutoff layer to obtain information about size and the poloidal rotation velocity of electron density fluctuations in the vicinity of the cutoff layer. A microwave is launched from a transmitting antenna into the plasma at a finite tilt angle ϕ_{tilt} with respect to the normal of the cutoff layer. The incident beam is both reflected and back scattered at the cutoff layer and the relation between the probing wave number k_0 and the wave number k of the density fluctuations responsible for the back scattering is given by the Brag diffraction equation for the back scattered wave. By varying the tilt angle ϕ_{tilt} the reflectometer is able to select plasma density fluctuations with finite wave number k in the cutoff layer. When the reflectometer is absolutely calibrated the amplitude of the detected wave can provide information of the density fluctuation level. Therefor by scanning the tilt angle it is possible to determine the fluctuation level of the density fluctuations with different k-values. The average perpendicular velocity of the selected electron density fluctuations is derived from the Doppler frequency shift between the outgoing and back scattered wave. This Doppler frequency

shift is induced by the movement of the selected density fluctuation $f_D = 1/(2\pi)v \cdot k$ where v is the rotation velocity. It is well known that the parallel wave number for tokamak fluctuations is small compared to the perpendicular wave number so the Doppler shift results only from the velocity component of the fluctuations perpendicular to the magnetic field $f_D = 1/(2\pi)v_\perp \cdot k_\perp$. The perpendicular velocity of the density fluctuations consist of two contributors: $\mathbf{v}_\perp = \mathbf{v}_{E_r \times B} + \mathbf{v}_{phase}$ where $\mathbf{v}_{E_r \times B}$ is the plasma rotation velocity relative to the lab frame and $\mathbf{v}_{phase}$ the phase velocity of the density fluctuation in the plasma frame. When the plasma is in an equilibrium state, no modulations in the phase velocity are expected and changes in the radial electric field dynamics will lead to a direct change in $f_D(t)$.

The back scattered radiation is detected by a microwave two-homodyne receiver detector. This detector provides both phase and amplitude information of the back scattered signal and the spectrum of the back scattered signal can be produced in the positive and negative frequency ranges by means of Fourier transformation of the complex signal of the detector $I(t) = \mathrm{Icos}(t) + i\mathrm{Isin}(t)$. This output signal of the Doppler Reflectometer detector can be related to density fluctuations by:

$$I(t) = \int\int \delta n(r, \theta, t) W(r, \theta) r dr d\theta \tag{3.1}$$

where $W(r, \theta) = \mathrm{Wcos}(r, \theta) + i\mathrm{Wsin}(r, \theta)$ is a complex spatial weighting function, $\delta n(r, \theta, t)$ the density fluctuation. The weighting function provides information on the spatial and wave number resolutions of the DR and depends on the antenna tilt angle with respect to the microwave cutoff layer. The Born approximation for axisymmetric distributions of the background plasma density, i.e. an approximation of small plasma fluctuations, has been used while constructing the weighting function. Where normally equation 3.1 is used to obtain information of density fluctuations from the DR detector signal it can also be used inversely. When density fluctuation information is provided equation 3.1 can reproduce the DR output signal by multiplication and spatial integration of the density fluctuations with the weighting function providing the synthetic diagnostic for DR spectra. The average shift of the spectrum is determined by the macro scale background flow where as the spectral shape is determined by the diagnostic instrument function together with the perturbations of the poloidal flow on both meso and micro scale level.

The FT-2 tokamak is equipped with two reflectometers: the Doppler Reflectometry (DR) [40] and the Doppler Enhanced Scattering (ES) [40, 41] microwave diagnostics. Both diagnostics utilize back scattering of electromag-

Table 3.1. Specifications of the microwave diagnostics

Microwave diagnostic	Doppler reflectometry	Enhanced scattering
Propagation	Ordinary	Extraordinary
Incident freq.	26-36 GHz	54-66 GHz
k_θ range	3-5 cm^{-1}	15-30 cm^{-1}
radial domain	0.8-0.9 r/a	0.65-0.87 r/a
rad. resolution	$\approx$ 0.5 cm	$\approx$ 0.1 cm

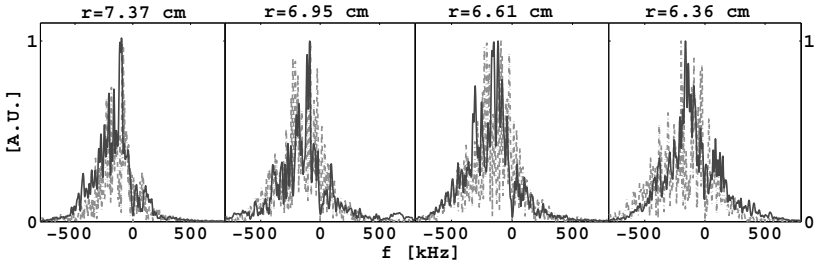

Figure 3.1. DR spectra (-) compared to the corresponding synthetic Doppler spectra (- ·) from the Elmfire simulation including impurities at several radial positions. ©American Physical Society

netic waves off low frequency small-scale density fluctuations in the vicinity of the cutoff for DR or the Upper Hybrid Resonance (UHR) layer for ES to obtain information about small-scale fluctuation spectra and their perpendicular rotation. Characteristics of the two microwave systems including their spatial and wavenumber resolutions for the simulation parameters given in publication VII are presented in TABLE I. Due to the fact that $B_\phi/B_\theta \gg 1$ the perpendicular motion of the density fluctuations is mainly in the poloidal direction. The Elmfire code resolves for density fluctuations larger than the ion Larmor radius which does not include the range of fluctuations responsible for probing wave back-scattering in the UHR, diagnosed by the ES diagnostic. As such the current version Elmfire code can not be used to investigate frequencies and wavenumber spectra but can be used to study E_r dynamics observed by the ES diagnostic. Synthetic Doppler spectra can not be produced for the ES diagnostic with the Elmfire code.

Comparisons of the shape between the reconstructed and the experimental DR frequency spectra at several radii are shown in figure 3.1 where the statistical averages on the saturated nonlinear state are performed over 64 μs to obtain similar statistics. Unfortunately the DR diagnostic at FT-2 is not absolutely calibrated and can not scan the turbulence k-spectrum by changing

Radius [cm]	7.34	7.17	7.06	6.90	6.61	6.50	6.36
v_θ COM [km/s]	-3.22	-2.43	-2.59	-1.99	-2.46	-2.20	-2.10
v_θ Gauss [km/s]	-2.98	-2.62	-2.48	-2.19	-2.73	-2.11	-2.08

Table 3.2. The average poloidal velocity obtained from the Centre-Of-Mass (COM) technique and the maximum of the Gaussian fit of the experimental Doppler spectrum.

its antenna tilt angle. Therefore comparisons of the turbulence fluctuation level at different k-values by comparing the spectral amplitude, as performed in [31], is not possible. The focus has therefore been on validating the poloidal flow dynamics by investigating large-scale mean $E \times B$ flows, fine-scale zonal flows and turbulence. This type of investigation requests that the total distribution function (full-f) is evaluated in time, as all the above mentioned processes have to be simultaneously incorporated into one simulation. In figure 3.1 not only the frequency shift, but also the width and even the form of the experimental spectra are well reproduced by the synthetic diagnostic indicating comparable rotation and spreading of the selected turbulent density fluctuations. To obtain the average fluctuation poloidal rotation velocity from the spectrum one can fit a Gaussian peak to the spectrum or use the centre-of-mass technique. In table 3.2 both values are shown.

In figure 3.2 average fluctuation poloidal rotation velocity obtained via the centre-of-mass technique is presented for the synthetic and measured spectrum and close agrement is found. The value, however is slightly higher than the computed $v_{E_r \times B}$ plasma rotation profile averaged over the DR domain. This should be attributed to the fluctuation phase velocity, which appears to be smaller than the plasma rotation velocity. The poloidal velocity of drift

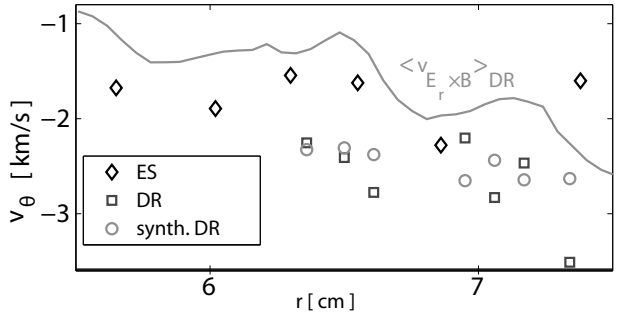

Figure 3.2. The poloidal velocity obtained from the ES (◊) and DR (□) measured frequency spectra and the synthetic DR spectra (o) compared to the $v_{E_r \times B}$ averaged over the DR domain. ©American Physical Society

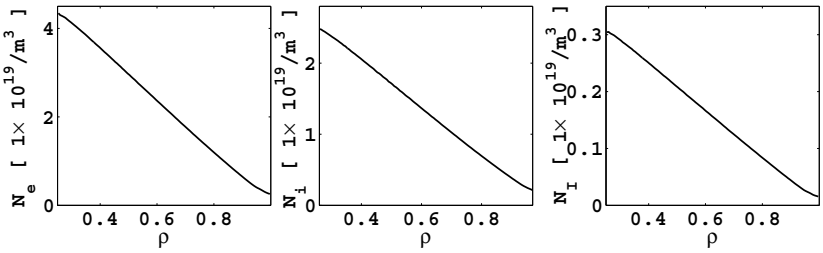

Figure 3.3. The electron, ion and impurity density profile for simulation VII

wave fluctuations responsible for probing wave back-scattering in the UHR can equally be obtained from the mean value of the ES Doppler frequency shift and is also included in figure 3.2. These velocities appear to be close to those given by DR, indicating similar poloidal velocities for density fluctuations with different poloidal wave numbers leading to the conclusion that for both diagnostics the $v_{E_r \times B}$ plasma rotation is larger than the phase velocity.In the next section the computed radial electric field E_r is investigated in more detail. The ES diagnostic at the FT-2 tokamak does provide the possibility to scan the tilt angle during a plasma discharge and in publication IV the frequency and wavenumber spectra of small-scale micro turbulence measured with the enhanced scattering diagnostic are presented. The linear growth rate and frequency of unstable drift modes responsible for UHR propagation are investigated with the gyrokinetic GS2 code [32]. For the plasma periphery a correlation between the small-scale component of the turbulence radial wave number spectrum and the TEM growth rate was found, leading to a conclusion that the radial wave number spectrum is formed by a cascade from the small wave number spectrum produced by the TEM instability rather than the ETG instability.

3.2 The background radial electric field

In this section the effect of the impurity ratio, the T_e/T_i ratio and the ion orbit losses on the background $E_r \times B$ flow are clearly illustrated by a set of parameter scans performed with the Elmfire code. The purpose of the parameter scans is to provide a better insight in the processes that determine the background radial electric field presented in the previous section and publication VII. An overview of the different simulations and their initialized parameters is given in Table 3.3.

In simulations 1-5 neoclassical filtering has been applied by removing modes

Table 3.3. Specifications for Elmfire simulations

Number	Neoclassical Filtering	T_e/T_i	Total plasma current [kA]	Z_{eff}
1	yes	1	55	1
2	yes	3	55	1
3	yes	1	55	3.1
4	yes	3	55	3.1
5	yes	3	18.9	3.1
6	no	3	18.9	3.1

with toroidal mode number $n \neq 0$ from the simulation at every timestep, prohibiting turbulent modes from developing while still recovering the poloidal side bands of the toroidal mode number $n = 0$. The temperature profiles are given in publication VII, where the T_e profile is set equal to the T_i profile when $T_e/T_i = 1$. The initialized electron, ion and impurity density profile for simulation VII are presented in figure 3.3. When no impurities are taken into account the initialized ion density is equal to the electron density presented in figure 3.3. The initialized impurity temperature is set to be equal to the initialized main ion temperature. For the presented profile parameters the main ions are in the plateau regime at the inner region of the simulation and in the Pfirsch-Schlüter regime at the outer region. The impurity ions are everywhere in the Pfirsch-Schlüter collisional regime. The banana orbit width varies between < 1 cm for simulations with total current of 55 kA to ≈ 2 cm for simulation with a total plasma current of 18.9 kA.

3.2.1 A relation between the ion flow velocity and E_r

Galeev and Sagdeev [33] derived the ion and electron fluxes, for arbitrary radial electric field, directly from the drift kinetic equation. Generalizing their analysis to include temperature gradient gives the following expression for the neoclassical particle flux for species α [34]:

$$\Gamma_\alpha^N = -n_\alpha D_\alpha \left(\frac{n'_\alpha}{n_\alpha} + \gamma_\alpha \frac{T'_\alpha}{T_\alpha} - \frac{q_\alpha}{T_\alpha} \left(E_r - B_p U_{\alpha\|} \right) \right) \tag{3.2}$$

with D_α the particle diffusion coefficient, γ_α a factor depending on the collisionality and $U_{\alpha\|}$ the flow velocity parallel to the magnetic field. Using the ambipolar condition for the neoclassical particle fluxes $q_i\Gamma_i + q_e\Gamma_e = 0$ and using the fact that $D_e \ll D_i$ the well-known relation between the parallel ion flow velocity and the radial electric field is obtained:

$$E_r = \frac{T_i n_i^{'}}{q_i n_i} + \gamma \frac{T_i^{'}}{q_i} + B_p U_{i,\parallel} = E_{NC} \tag{3.3}$$

In figure 3.4 the flux-surface-averaged radial electric field for simulations 1 and 2 are presented and compared to E_{NC}. For γ the ν_* approximate fit as given by Hinton *et al.* [42] is used:

$$\gamma = 1 - \frac{\left(\frac{1.17-0.35\sqrt{\nu_*}}{1+0.7\sqrt{\nu_*}}\right) - 2.1\nu_*^2\epsilon^3}{1+\nu_*^2\epsilon^3} \tag{3.4}$$

A good agreement is found everywhere except near the outer border for both cases, proving that the neoclassical electron flux can be ignored even when the gradient of the electron temperature is higher than the ion temperature gradient due to $T_e = 3T_i$ and the equation for E_{NC} holds. The discrepancy near the outer boundary will be discussed in more detail, when the ion orbit loss effect on E_r is studied in section 3.2.3.

3.2.2 The influence of impurities on the plasma flow

When impurity ions are included in the simulation the flux-surface-averaged radial electric field no longer converges to E_{NC}, as shown in figure 3.5. When the radial gradients of the density and temperature are rather steep, as is the case for the presented FT-2 simulations, a poloidal variation in the density of the impurities can arise. This variation can lead to a substantial modification of the radial electric field compared to the conventional description E_{NC}. The influence of impurities on the plasma flow when the bulk ions are in the plateau collisionality regime and the impurities in the Pfirsch-Schlüter collisionality regime is addressed by Landreman *et al.* [43]. A correction factor to E_{NC} is defined as:

$$X = \left(1+\frac{\eta}{2}\right)^{-1}\left\{1 + \frac{\eta y}{2}\left\langle nb^2\right\rangle - \left[3+(1+y)\tau_*\right]\epsilon\eta\left\langle n\cos\theta\right\rangle\right\} \tag{3.5}$$

where

$$y = \frac{Z\epsilon^2\tau_*\alpha^{-1} + \eta^{-1}(\left\langle n/b^2\right\rangle - 1) - 3\epsilon\left\langle nb^{-2}\cos\theta\right\rangle + (3+\tau_*)\epsilon\left\langle n\cos\theta\right\rangle}{Z\epsilon^2\tau_*\alpha^{-1} + 2^{-1}\left(\left\langle nb^2\right\rangle - 1\right) - \epsilon\tau_*\left\langle n\cos\theta\right\rangle} \tag{3.6}$$

with $\eta = p_i T_i^{'}/(p_i^{'} T_i)$, $\alpha = \langle n_Z\rangle T_0 Z^2/(2n_0 T_i)$, $2n_0/T_0 = n_{e0}/T_e + n_{i0}/T_i$ and ϵ the inverse aspect ratio. The normalized collisionality is defined as:

$$\tau_* = \frac{\sqrt{\pi} Z T_0 \tau_{iZ} n_Z v_i B\cdot\nabla\theta}{8 T_i n_0 B_0} \tag{3.7}$$

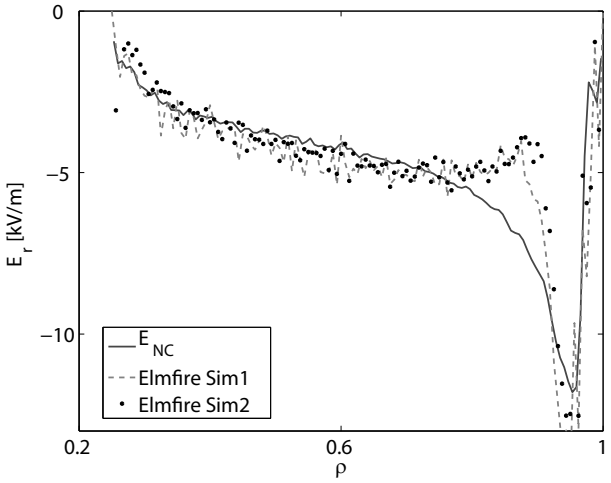

Figure 3.4. The flux-surface-averaged radial electric field obtained with the Elmfire code compared to the analytical estimate E_{NC} for simulations 1 ($T_e/T_i = 1$, $Z_{eff} = 1$, $I_t = 55$ kA) and simulation 2($T_e/T_i = 3$, $Z_{eff} = 1$, $I_t = 55$ kA).

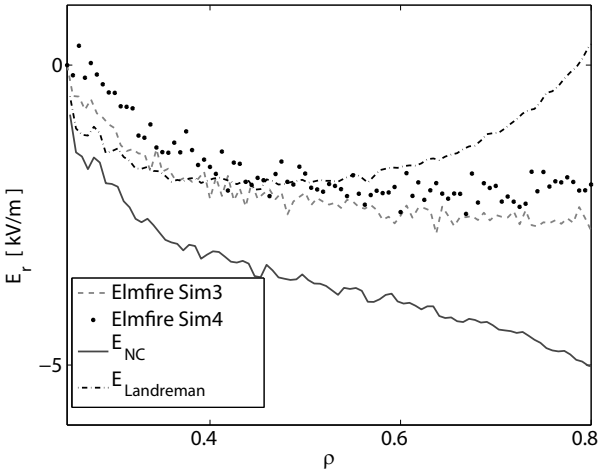

Figure 3.5. The flux-surface-averaged radial electric field obtained with the Elmfire code compared to the analytical estimates E_{NC} and the approach presented by Landreman *et al.* for simulations 3 ($T_e/T_i = 1$, $Z_{eff} = 3.1$, $I_t = 55$ kA) and simulation 4 ($T_e/T_i = 3$, $Z_{eff} = 3.1$, $I_t = 55$ kA).

with $\tau_{iZ} = 3(2\pi T_i)^{3/2}\epsilon_0^2 m_i^{1/2}/(n_Z Z^2 q_e^4 \lambda_{iZ})$ where λ_{iZ} is defined in equation 2.22. The weak density variation approach is used by expanding the density as $n = 1 + n_c \cos\theta + n_s \sin\theta$ with:

$$n_s = \epsilon g(1+\alpha)\frac{2-\eta\left[3+(1+y)\tau_*\right]}{(1+\alpha)^2 + g^2(1+\eta y/2)^2} \tag{3.8}$$

$$n_c = -\epsilon g^2(1+\eta y/2)\frac{2-\eta\left[3+(1+y)\tau_*\right]}{(1+\alpha)^2 + g^2(1+\eta y/2)^2} \tag{3.9}$$

and

$$g = -\frac{m_i I p_i^{'}}{q_e T_i \tau_{iZ} n_Z B \cdot \nabla\theta} \tag{3.10}$$

The flux-surface-averages in equation 3.5 and 3.6 are defined by

$$\left\langle nb^{-2}\right\rangle = \langle n(1+2\epsilon\cos\theta)\rangle \tag{3.11}$$

$$\left\langle nb^{-2}\cos\theta\right\rangle = \langle n(1+2\epsilon\cos\theta)\cos\theta\rangle \tag{3.12}$$

$$\left\langle nb^{2}\right\rangle = \langle n(1-2\epsilon\cos\theta)\rangle \tag{3.13}$$

In figure 3.5 the radial electric field E_{NC} multiplied by the correction factor X is compared to the Elmfire simulation results. A good agreement is found for the inner side of the radial simulation domain. When moving to the outside of the radial simulation domain the discrepancy between the analytical Landreman approach and the Elmfire simulation result increases exponentially. This discrepancy can be explained by the main ion collisionality regime to shift from the plateau collisionality regime to the Pfirsch-Schlüter regime for which the Landreman approach is no longer valid. It is interesting to notice that when $T_e = 3T_i$ and impurities are included in simulation 4 a small increase of the radial electric field is observed. This can be explained by the fact that apart from the electron temperature gradient being higher than the ion temperature gradient, the electron density gradient is now also higher than the ion density gradient resulting in a small contribution of the electron flux.

3.2.3 The ion orbit loss effect on E_r

In publications [44, 45] a clear influence of nonambipolar ion orbit losses on the radial electric field is observed near the outer boundary. By decreasing the total plasma current the banana orbit width can be increased and the penetration depth of the ion orbit loss effect can be investigated. In figure 3.6 the radial electric field of simulation 4 with a total current of 55 kA and simulation 5 with a total current of 18.9 kA are compared. It can be clearly seen

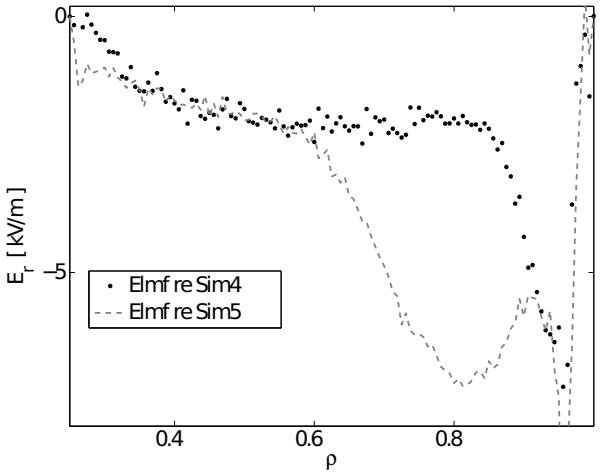

Figure 3.6. The flux-surface-averaged radial electric field obtained with the Elmfire code for simulations 4 ($T_e/T_i = 3$, $Z_{eff} = 3.1$, $I_t = 55$ kA) and simulation 5 ($T_e/T_i = 3$, $Z_{eff} = 3.1$, $I_t = 18.9$ kA), illustrating the ion orbit loss effect by varying the total plasma current.

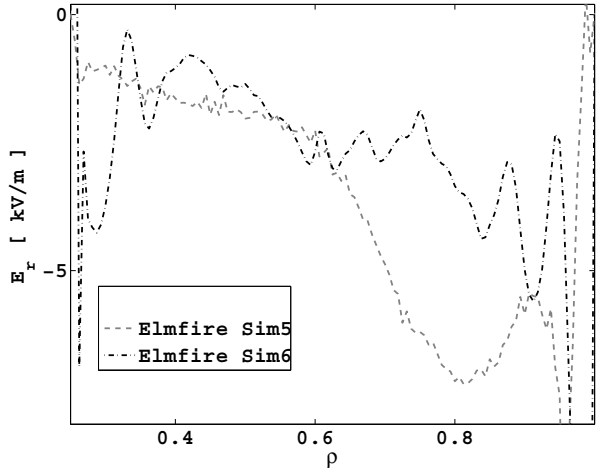

Figure 3.7. The flux-surface-averaged radial electric field obtained with the Elmfire code for simulation 5 (Neoclassical filtering) and simulation 6 (no neoclassical filtering), illustrating the effect of turbulent transport on the ion orbit loss effect.

that the lower the current the further the ion orbit loss effect on the radial electric field penetrates into the simulation domain and the absolute radial electric field value becomes strongly enhanced. As such it can be concluded that the ion orbit loss effect near the outer boundary plays a substantial role in explaining the observed discrepancy at the outer boundary between E_{NC} and the Elmfire radial electric field, discussed in section 3.2.1. It is interesting to note that when turbulence is allowed to develop in simulation 6, the effect of the ion orbit losses on the radial electric field seems to disappear, as shown in figure 3.7. In this figure the radial electric field from the simulation including turbulence is averaged over 64 μs to remove the turbulence driven radial electric field fluctuations. The fact that the ion orbit loss process is such a slower process compared to the particle losses due to turbulent transport could explain this observation.

3.3 Turbulent transport in the FT-2 tokamak

Apart from collisional transport also turbulent transport is present in a tokamak and in most plasmas the turbulent transport is far larger than the neoclassical transport. This same observation has been made for ohmic FT-2 discharges where the neoclassical and turbulent heat conductivity and diffusion coefficient obtained with Elmfire simulations are presented in figure 1 of publication VII. As such, it can be stated that in general the neoclassical model provides a lower limit for the tokamak transport. Turbulent transport results from plasma fluctuations in an inhomogeneous plasma. The fluctuations are able to grow when the gradients of the temperature and/or density are able to provide free energy to the fluctuations. While the fluctuations are growing bigger nonlinear terms will enable energy exchange between various turbulent modes which will limit the growth of the originally linear turbulent modes, leading to a saturated turbulent state of the plasma. Depending on the plasma parameters various turbulent instabilities exist and in a tokamak plasma micro instabilities of the size of the Larmor radius $k_\perp \rho_s \sim 1$ with growth rates of the order of the diamagnetic frequency are responsible for the observed turbulent transport.

3.3.1 The linear growth rate of drift wave instabilities

The two most common micro instabilities with the appropriate time a spatial scales are the Ion Temperature Gradient (ITG) mode and the Trapped

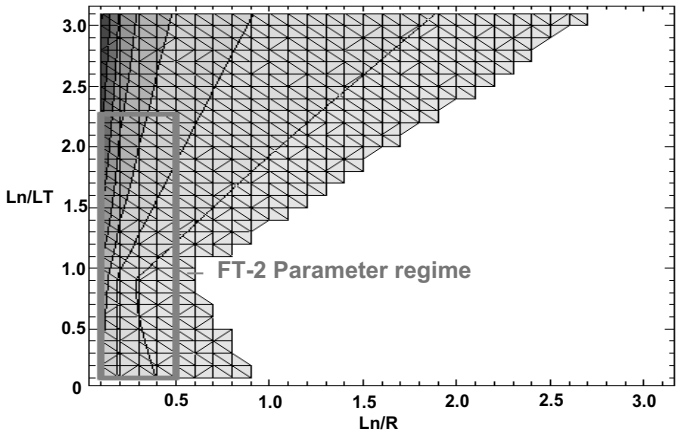

Figure 3.8. The area of positive (black) and negative (white) growth rates calculated with the Weiland model for simulation case 1 at $\rho = 0.65$.

Electron Mode (TEM). In an inhomogeneous magnetic field both of these instabilities are driven by the curvature and gradient drift of the magnetic field:

$$v_{D\alpha} = \frac{T_\alpha}{m_\alpha \Omega_\alpha} \mathbf{b} \times (\mathbf{b} \cdot \nabla \mathbf{b} + \nabla \ln B) \tag{3.14}$$

In the following we assume the plasma to be quasi neutral $\delta n_i = \delta n_e$ and we start by treating the electron perturbation adiabatically $\delta n_e / n_e = e\phi / T_e$. When a temperature perturbation occurs in the poloidal direction at the outboard plane of the tokamak the magnetic field gradient and the ion temperature gradient point in the negative radial direction. Because the $v_{D\alpha}$ drift is depending on both the temperature and the magnetic field gradient the fast ions with high temperature will travel faster than the colder ions, causing a density perturbation. The density perturbation will transfer via the adiabaticity of the electrons to a potential fluctuation, which will cause a $E \times B$ drift enhancing the initial perturbation, driving the ITG instability unstable. At the inboard plane of the tokamak the magnetic field gradient and the ion temperature gradient are in opposite directions which stabilizes the instability. When there is a trapped fraction of electrons, the thermalisation along the magnetic field line is distorted and poloidal temperature perturbations can occur. These perturbations will provide a similar instability as described for the ITG instability, with the difference that now only the passing fraction of the electrons will provide the adiabatic response to the potential fluctuation.

In this section the Weiland reactive fluid model [46] is used to find an estimate for linear growth rates and frequencies for ITG and TEM drift instabilities in FT-2 ohmic discharges. The model starts from the moments of the Fokker Planck equation presented in section 1.2 by treating the fluctuations as first order corrections of the distribution function. The equations are linearized by assuming $T = T_0 + \delta T$ and $n = n_0 + \delta n$ and Fourier analyzed by transforming $\nabla \rightarrow i\mathbf{k}$ and $\partial/\partial t \rightarrow -i\omega$. The fluid velocity for species α is defined as:

$$\mathbf{v}_\alpha = \mathbf{v}_{*\alpha} + \mathbf{v}_{E\alpha} + \mathbf{v}_{\pi\alpha} + \mathbf{v}_{p\alpha} \tag{3.15}$$

$$= \frac{\mathbf{b}\times\nabla p_\alpha}{n_\alpha m_\alpha \Omega_\alpha} + \frac{\mathbf{E}\times\mathbf{b}}{B} + \frac{\mathbf{b}\times\nabla\cdot\mathbf{\Pi}_\alpha}{n_\alpha m_\alpha \Omega_\alpha} + \frac{1}{\Omega_\alpha B}\frac{d\mathbf{E}}{dt} \tag{3.16}$$

where $\mathbf{v}_{*\alpha}$ is the diamagnetic drift, $\mathbf{v}_{E\alpha}$ the $E\times B$ drift, $\mathbf{v}_{\pi\alpha}$ the viscosity drift and $\mathbf{v}_{p\alpha}$ the polarization drift. From the continuity equation and the energy balance while using the diamagnetic closure for the heat flow the following dispersion relation for the ITG and TEM instabilities can be derived:

$$\frac{\omega_{*e}}{N_i}\left[\omega(1-\epsilon_n) + \left(\eta_i - \frac{7}{3} + \frac{5}{3}\epsilon_n\right)\omega_{Di} - k^2\rho_s^2\left[\omega - \omega_{*i}(1-\eta_i)\right]\left(\frac{\omega}{\omega_{*e}} + \frac{5}{3\tau}\epsilon_n\right)\right]$$
$$= f_t\frac{\omega_{*e}}{N_e}\left[\omega(1-\epsilon_n) + \left(\eta_e - \frac{7}{3} + \frac{5}{3}\epsilon_n\right)\omega_{De}\right] + 1 - f_t \tag{3.17}$$

with $\omega_{D\alpha} = \mathbf{v}_{D\alpha}\cdot\mathbf{k}$, $\omega_{*\alpha} = \mathbf{v}_{*\alpha}\cdot\mathbf{k}$, $\epsilon_n = 2L_n/L_B$, $\eta_a = L_{na}/L_{Ta}$ where $L_B = B/|\nabla B|$ is the magnetic field gradient length, $L_{n\alpha} = n_\alpha/|\nabla n_\alpha|$ the density gradient length, $L_{T\alpha} = T_\alpha/|\nabla T_\alpha|$ the temperature gradient length, $\tau = T_e/T_i$, f_t the trapped particle fraction as defined in section 1.1 and $N_\alpha = \omega^2 - \frac{10}{3}\omega\omega_{D\alpha} + \frac{5}{3}\omega_{D\alpha}^2$ where α denotes the particle species. If $N_i - N_e < 0$ the mode is defined as the ion temperature gradient mode and travels in the ion diamagnetic direction. If $N_i - N_e > 0$ the mode is defined as the trapped electron mode and travels in the electron diamagnetic direction. The dispersion relation 3.17 can be solved easily for a certain $k\rho_i$ interval by varying ϵ_n and η_a. The obtained eigenvalues can be expressed as $\omega = \omega_r + i\gamma$, where ω_r is the frequency and γ the linear growth or damping rate of the Fourier mode. Positive growth rates describe a growing unstable mode where as stable modes have negative growth rate. In figure 3.8 the highest growth rate for each point in the (ϵ_n,η_i) plane is plotted for $\tau = 1$, $L_B = R_0^{-1}$ and $k_\perp\rho_i = 0.1 - 1$. The negative growth rates are set to zero, so the white area indicates the stable domain. For all the positive growth rates $N_i - N_e > 0$ indicating that the trapped electron mode is unstable and the modes are propagating in the

electron diamagnetic direction. In [47] figure 3.8 is presented for $\tau = 2,3$ showing an increase of the positive growth rate domain in both the ϵ_n and η direction. In the same work a wide variety of FT-2 discharges are analyzed and the parameter regime of all these discharges is indicated by the red square in figure 3.8. For all of the analyzed FT-2 discharges $\eta < 0.5$ was found indicating that there is no FT-2 parameter regime for which the trapped electron mode is stable. A similar linear growth rate and frequency analysis has been performed while using the GS2 code [32] and also here for none of the discharges a negative growth rate was found for the $k_\perp \rho_i = 0.1 - 0.6$ domain and the mode propagation was always in the electron diamagnetic direction. These analysis support the Elmfire results for the phase velocity presented in publication II, III and VII where a phase velocity of the density fluctuations in the electron diamagnetic direction was found.

3.3.2 E_r dynamics in turbulent FT-2 plasmas

It is widely believed that transport of momentum via turbulent Reynolds stresses can generate an amplification of $E \times B$ zonal flows [48] which can lead to a decorrelation of turbulent eddies, decreasing the radial transport. Zonal flows distinguish themselves from the mean $E_r \times B$ flows by capturing their energy exclusively via nonlinear transfer from drift wave turbulence. Zonal flows therefore vanish when the underlying drift wave drive is extinguished in contrary to the mean $E_r \times B$ flows discussed in section 3.2 which are also present in the absence of turbulence. The zonal flows are electrostatic potential fluctuations with zero toroidal mode number and finite radial wavenumber and can be categorized in two branches: the zero frequency branch and the high frequency branch which involves an m=1 pressure disturbance. The pressure disturbance is known as the Geodesic Acoustic Mode (GAM).

As described in section 3.1, publication III and publication VII the poloidal flow of density fluctuations can be studied with reflectomtery diagnostics and in figure 3.2 the measured averaged poloidal flow was compared to the simulated predictions. It has so far been impossible to clarify whether the first branch of the zonal flow is creating any changes to the equilibrium $E \times B$ flow due to the lack of an accurate analytical or numerical model to predict the mean $E \times B$ flow in the outer region of the simulation domain. A good agreement however is found between the measured and simulated averaged poloidal rotation, indicating that the observed increased radial electric field due to ion orbit losses as observed in figure 3.7 is most certainly not seen by experiments. This supports the conclusion that turbulence driven radial

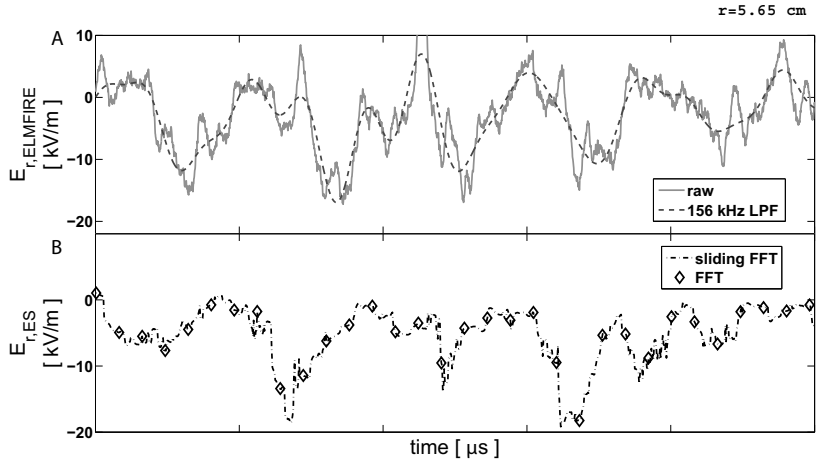

Figure 3.9. A) The simulated raw (-) and low pass filtered (- -) radial electric field time trace averaged over the ES domain centered at r=5.6 cm for the turbulent saturated stage. B) The radial electric field measured by ES at r=5.6 cm analyzed with FT (◊) and sliding FT (- ·). ©American Physical Society

particle fluxes eliminate the ion orbit loss effect on the equilibrium $E \times B$ flow observed in neoclassical simulations.

In publication VII the spectral width of the DR spectrum is explained, in substantial part, by giant oscillations of the field at a frequency of approximately 30-50 kHz much smaller than the typical drift wave frequency, but much larger than the inverse energy confinement time, attributed to the geodesic acoustic mode (GAM). This is supported by DR and ES measurements revealing similar oscillations in the poloidal velocity meso-scale dynamics. Applying the sliding Fourier Transform (FT) procedure and the δ-phase method presented by Conway at al. [52] to the time signals obtained by the backscattering techniques $f_D(t)$ time sequences are generated which by Fourier analysis give the E_r spectrum and reveal the GAM like spectral lines. In figure3.10B the dominant E_r oscillation frequency dependence on the radius obtained by Elmfire simulations with and without impurities, the ES and DR measurements are presented. The Geodesic Acoustic Mode can be described by a dispersion relation for which the angular frequency including the impurity contribution has been recently presented by Guo *et al.* [53] and is given by:

$$\omega \approx \left[\frac{2T_i}{R^2} \left(\frac{\frac{7}{4}(n_i + n_z) + A}{n_i m_i + n_z m_z} \right) \right] \tag{3.18}$$

with

$$A = n_i \tau_i \frac{n_i q_i}{q_e n_e} + n_z \tau_z \frac{n_z q_z}{q_e n_e} + n_i \frac{q_i}{q_z} \tau_z \frac{n_z q_z}{q_e n_e} + n_z \frac{q_z}{q_i} \tau_i \frac{n_i q_i}{q_e n_e} \tag{3.19}$$

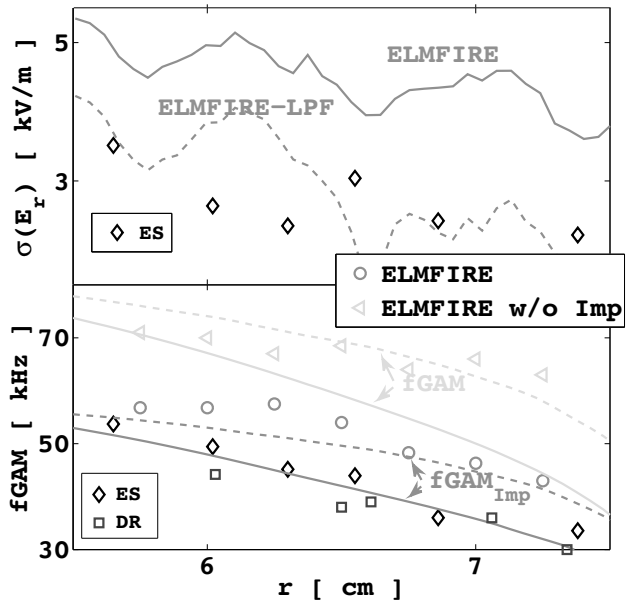

Figure 3.10. Upper) The standard deviation of the simulated raw (-) and LP-filtered (--) radial electric field fluctuations averaged over the ES domain compared to the ES measurements. Lower) The dominant frequency of the ES (◊) and DR (□) measured radial electric field fluctuations compared to the Elmfire predictions with (o) and without impurities (△) included. The analytical predictions for the geodesic acoustic frequency with (pink) and without impurities (green) are presented for the start up (-) and steady state (--) profiles. ©American Physical Society

where $\tau_{i/z} = q_{i/z}T_e/(q_eT_{i/z})$. This analytical value for the GAM frequency is also included in figure 3.10B. For both the Elmfire simulations with and without impurities, the dominant frequency is fairly reproduced by Guo's analytical theory whereas a good match of Guo's theory to the ES and DR results is found when the O^{+6} impurity component is accounted for.

More detailed investigations of the $E_r(t)$ oscillations were performed while using the Doppler ES diagnostic, which possesses a much better spatial resolution and higher GAM spectra peak contrast (≈ 4) then the DR. The radial electric field time trace obtained with the Doppler ES technique is shown in figure 3.9B. This $E_r(t)$-signal, was constructed from scattering spectra with an FT window of 64 points and a sampling period of 50 ns, corresponding to a Nyquist frequency of $f_N = 156.25$ kHz. For one on one comparison, frequencies above the Nyquist frequency are removed from the simulated E_r time trace by a 156 kHz Low Pass Filter (LPF), as demonstrated by the dotted line in figure 3.9A. The probability distribution functions of radial electric field fluctuations $\delta E_r(t) = E_r(t) - \langle E_r(t)\rangle_t$, where $\langle E_r(t)\rangle_t$ is the time averaged mean, at the radial position presented in figure 3.9 are shown to be similar and well

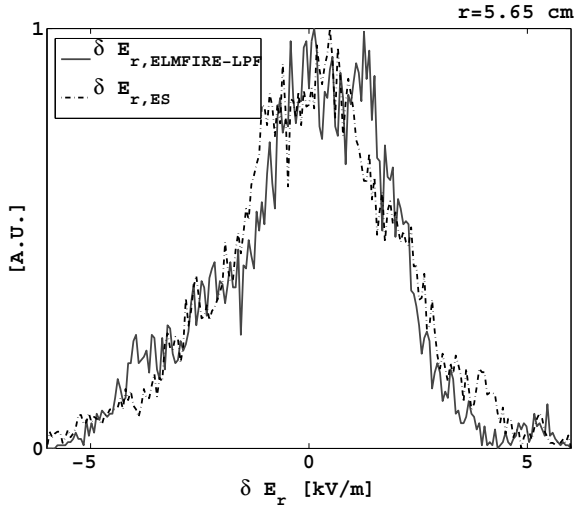

Figure 3.11. The probability distribution function of the simulated LP filtered (-) and sliding FT ES (- ·) measured radial electric field fluctuations at r=5.6 cm. ©American Physical Society

approximated by normal law, as shown in figure 3.11. This illustrates well the stochastic nature of the GAM fluctuations. The standard deviation of the δE_r probability distribution functions at various radial positions is presented in figure 3.10A. At all radial positions a good agreement is found between the simulated and experimental standard deviation when filtering is applied to the simulated data. When no filtering is used on the simulated E_r, the fluctuations have significantly higher average amplitudes. It can be concluded that the simulations predict the correct GAM E_r amplitude, even though the GAM frequency is slightly over predicted. This over prediction can be explained by the increased steady state temperature profiles caused by the under prediction of edge transport.

4. Summary & Future prospects

Numerical simulations of plasma turbulence performed with the Elmfire full-f gyrokinetic particle-in-cell code for ohmic heated discharges from the small FT-2 tokamak are presented. Resolution and conservation requirement of the simulations are discussed and questions concerning the validity of the theoretical background of the Elmfire code have been answered (see publication V). The importance of the new momentum conserving interpolation scheme, presented in publication VI, is clearly illustrated in section 2.3.3 by illustrating its influence on the radial transport coefficients and the radial electric field. The spatial resolution and test particle number requirements have been addressed in section 2.4 and 2.7, respectively. It was proven that an average of 3000 test particles is enough to work above the noise level and that the shear is correctly recovered when a grid resolution of 120/150/8 in radial/poloidal/toroidal direction is used for the simulation presented in publication VII.

Publication I and II present the first preliminary Elmfire simulation results of the radial electric field dynamics and the poloidal velocity for ohmic FT-2 tokamak discharges in the presence of micro turbulence. A good agreement of the E_r profile was found to neoclassical predictions at the plasma core, but not at the edge of the plasma. It was shown that fluctuation driven neoclassical non-ambipolar finite Larmor radius effects were insufficient to explain the observed deviation at the edge, however Reynolds stress driven by turbulence eddy viscosity and/or the geodesic acoustic mode was suggested as a possible explanation. In [54] the radial electric field results of publication I are reassessed while using the momentum conserving interpolation scheme. The suppression of the radial electric field near the outer edge is no longer observed and the radial electric field converges to its neoclassical prediction.

In publication III a weighting function synthetic diagnostic, based on full-wave electromagnetic wave propagation, is outlined to validate poloidal velocity of simulated density fluctuations to Doppler reflectometry (DR) measure-

ments. The main results of this manuscript are presented in publication VII where direct measurements of micro, meso, and macro-scale transport phenomena in ohmic FT-2 discharges are shown to be quantitatively reproduced by the Elmfire simulation predictions. It was proven that Elmfire simulations of an ohmic FT-2 discharge quantitatively reproduce estimations of the effective thermal diffusivities and the mean poloidal fluctuation rotation profile (macro scale), the GAM dynamics and E_r fluctuation statistics (meso scale) and the DR frequency spectra (macro, meso & micro scale) demonstrating the codes ability to simultaneously reproduce a wide range of transport scale levels accurately. Chapter 3 of the introductory part of this manuscript has been used to further strengthen the presented Elmfire results published in publication VII. In this chapter the measured and simulated mean equilibrium $E \times B$ flows are validated against various analytical models where the effect of $T_e > T_i$, ion orbit losses and impurities are investigated in more detail providing a more solid basis for the findings on the background flow presented in publication VII. It can now be concluded that impurities have an influence on both the mean $E \times B$ velocity as well as the burstiness of the observed $E \times B$ velocity dynamics. The linear growth rate results presented in section 3.3.1 support the Elmfire results for the phase velocity found in publication II, III and VII providing proof that the trapped electron mode is the dominant turbulent instability present in ohmic FT-2 discharges. The heat sources and sinks utilized in the simulation to obtain the steady state simulation profiles are described in section 2.6 and the Elmfire resistivity results are benchmarked to the Sauter model. No influence of turbulent transport on the resistivity was observed in the Elmfire simulation.

The predictive power of the full-f gyrokinetic code Elmfire is illustrated by reproducing the poloidal flow dynamics for an ohmic FT-2 discharge. These results could be strengthened in the near future by absolute calibration of the FT-2 DR diagnostic and upgrading the diagnostic to scan the tilt angle during a plasma discharge. This would make code validation of the turbulence fluctuation level at different k-values possible. Furthermore an effort could be made to upgrade the Elmfire model to resolve for density fluctuations smaller than the ion Larmor radius enabling validation against ES spectra. A module for lower hybrid heating is already present in the Elmfire code, and validation in this heating regime will be performed in the near future. Furthermore an in-depth coherence analysis of the ES GAM measurements are planned and radial correlation lengths and times will be compared to the Elmfire simulation predictions. Next to the FT-2 validation work, an effort to validate DR

results obtained at the mid-sized TEXTOR tokamak are scheduled for the upcoming year. First simulation results of the TEXTOR edge for a low and high confinement discharge are presented in publication VIII. Due to limited computational resources the simulations have so far been restricted to the edge plasma. A recent increment of available CPU hours and the upgrade of the memory handling scheme of the code will soon allow for simulations of the entire TEXTOR tokamak, making the implementation of realistic sources and sinks to prevent profile relaxation easier. Although Elmfire simulation of mid-sized tokamak now seems to be feasible, the road to accurately simulate plasma discharges of bigger machines like ASDEX upgrade, JET and ultimately ITER is still challenging. The large aspect ratio assumption for the magnetic field will no longer be valid and the inclusion of a more realistic magnetic field background will be necessary. In fact the analytical model presently used in the code might already not be accurately enough for mid-sized tokamaks. Furthermore the inclusion of electromagnetic perturbations has to be questioned, specially when simulations of the low to high confinement transition will be addressed. Both the magnetic field upgrade as well as the inclusion of magnetic field perturbation will ask for many changes to the Elmfire source code and will require more memory and CPU resources. Nevertheless it is the ultimate goal of the Elmfire code development group to address these problems in the near future.

Bibliography

[1] Adopted from M.J. Mantsinen,"Development and experimental evaluation of theoretical models for ion cyclotron resonance frequency heating of tokamak plasmas", Report TKK-F-A789, TKK, Espoo (1999)

[2] S.E. Parker, W.W. Lee, Phys. Fluids B5, 77 (1993)

[3] A.M. Dimits, G. Bateman, M.A. Beer, *et al.*, Phys. Plasmas 7, 969 (2000)

[4] Y. Chen, S. Parker, Phys. Plasmas 8, 2095 (2001)

[5] F. Jenko, W. Dorland, Plasma Phys. Control. Fusion 43, A141 (2001)

[6] J. Candy, R.E. Waltz, J. Comput. Phys 186, 545 (2003)

[7] Y. Idomura, S. Tokuda, Y. Kishimoto, Nucl. Fusion 43, 234 (2003)

[8] C.C. Kim, S.E. Parker, J. Comp. Phys. 161, 589 (2000)

[9] Z. Lin, W.W. Lee, Phys. Rev. E52, 5646 (1995)

[10] R.D. Sydora, Phys. Scr. 52, 474 (1995)

[11] L. Villard, S.J. Allfrey, A. Bottino,*et al.*, Nucl. Fusion 44, 172 (2004)

[12] G. Furnish, W. Horton, Y. Kishimoto, M. LeBrun, T. Tajima, Phys. Plasmas 6, 1227 (1999)

[13] M. Brunetti, V. Grandgirard, O. Sauter,*et al.* Comput. Phys. Commun. 163, 1 (2004)

[14] C.S. Chang, S. Ku, M. adams, *et al.* 21st IAEA Fusion Energy Conference, Chengdu, China, paper TH/P6-14 (2006)

[15] X.Q. Xu, Z.iong, M.R. Dorr, Nucl. Fusion 47,809 (2007)

[16] Y. Idomura, M. Ida, S. Tokuda, 34th EPS Conference on Plasma Physics, Warsaw, Poland, paper P-4.040 (2007)

[17] J.A. Heikkinen,S.J. Janhunen, T.P. Kiviniemi, F. Ogando, J. Comp. Phys. 227, 5582 (2008).

[18] P. Helander and D.J. Sigmar,*collisional Transport in Magnetized Plasmas*, Cambridge University press (2002)

[19] P.P. Sosenko, P. Bertrand, and V.K. Decyk, Physica Scripta 64, 264 (2001).

[20] F.I. Parra , P.J. Catto and S. Leerink, Polarization density in Elmfire, Internal report (2010).

[21] J.A. Heikkinen and M. Nora, Phys. Plasmas 18, 022310 (2011)

[22] L. Wang and T.S. Hahm, Phys. Plasmas 17, 082304 (2010)

[23] S. Leerink, F.I. Parra and J.A. Heikkinen, Phys. Plasmas 17, 124701 (2010)

[24] L. Wang and T.S. Hahm, Phys. Plasmas 17, 124702 (2010)

[25] J.A. Byers, A.M. Dimits, Y. Matsuda and A.B. Langdon, J. comput. Phys. 115, 352 (1994)

[26] R.B. White and M.S. Chance, Phys. Fluids 27, 2455 (1994)

[27] A.M. Dimits, Phys. Rev. E 48, 4070 (1993)

[28] B. Scott, private communications

[29] T. Takizuka and H. Abe, J. Comput. Phys. 25, 205 (1977)

[30] L. Spitzer, *Physics of Fully Ionized Gases*, Interscience, New York (1962)

[31] A. Casati, T. Gerbaud, P. Hennequin, *et al.*, Phys. Rev. Lett. 102, 165005 (2009)

[32] M. Kotschenreuther, G. Rewoldt, and W.M. Tang, Comp. Phys. Comm. 88, 128 (1995)

[33] A.A. Galeev and R.Z. Sagdeev, SOV. Phys.-JETP 26, 233 (1968).

[34] T.E. Stringer, Nuclear Fusion 35, 8 (1995)

[35] S.P. Hirshman, R.J. Hawryluk and B. Birge, Nuclear Fusion 17, 611 (1977)

[36] S. Hirshman and D. Sigmar, Physics of Fluids 20, 418 (1977)

[37] O. Sauter and C. Angioni, Phys. Plasmas 6, 2834 (1999)

[38] P. Niskala, Plasma Conductivity Comparison between Elmfire simulation code and analytical models, Special Assignment (2011)

[39] T.E. Stringer and J.W. Connor, Phys. Fluids 72, 2177 (1971)

[40] E.Z. Gusakov, A.D. Gurchenko, A.B Altukhov, Plasma Phys. Control. Fusion 48, B443 (2006)

[41] A.D. Gurchenko, E.Z. Gusakov, D.V. Kouprienko, *et al.*, Plasma Phys. Control. Fusion 52, 035010 (2010)

[42] F.L. Hinton and R.D. Hazeltine, Rev. Mod. Phys. 48, 240 (1976)

[43] M. Landreman, T. Fülöp, and D. Guszejnov, Phys. Plasmas 18, 092507 (2011)

[44] J.A. Heikkinen, T.P. Kiviniemi and A.G. Peeters, Plasma Phys. Contr. Fus. 40, 693 (1998)

[45] J.A. Heikkinen, T.P. Kiviniemi and A.G. Peeters, Phys. Rev. Lett. 84, 487 (2000)

[46] J. Weiland, *Collective modes in Inhomogeneous Plasma; Kinetic and Advanced Fluid Theory*, I.O.P. Publishing Ltd (2000)

[47] P. Niskala, Linear plasma instabilities in FT-2 tokamak, Bachelor Thesis, Aalto University (2011)

[48] P.H. Diamond,Plasma Phys. Control. Fusion 47, R35 (2005)

[49] P. Hennequin, R. Sabot, C. Honore, *et al.*, Plasma Phys. Control. Fusion 46, B121 (2004)

[50] A.D. Gurchenko, E.Z. Gusakov, A.B. Altukhov, *et al.*, Nucl. Fusion 47, 245 (2007)

[51] A.D. Gurchenko and E.Z. Gusakov, Plasma Phys. Control. Fusion 52, 124035 (2010)

[52] G.D. Conway, B. Scott, J. Schirmer, *et al.*, Plasma Phys. Control. Fusion 47, 1165 (2005)

[53] W. Guo, S. Wang and J. Li, Phys. Plasmas 17, 112510 (2010)

[54] S.J. Janhunen, PhD-thesis Aalto University (2013), to appear online in http://lib.tkk.fi/Diss

Nuclear Fusion could be used as a basis for clean commercial energy production in the near future. The tokamak magnetic confinement device has so far been most succesful in creating nuclear fusion conditions on earth. A major setback for creating fusion conditions in a tokamak is caused by turbulence induced transport which makes fuel particles to drift faster from the magnetic field lines than predicted by classical transport theory, disturbing the plasma confinement and thereby the fusion process. Low frequency turbulence-induced zonal flows along with large ExB flows however can decorrelate turbulent fluctuations leading to enhanced confinement regimes. Turbulent transport and in particular its self regulation can be studied with first principal computer models, which solve for the coupled problem of Bolzmann's kinetic equations and Maxwell's equations. In this manuscript turbulent transport phenomena in ohmic FT-2 tokamak discharges are modeled with the first principal code ELMFIRE.

Aalto-DD 176/2012

ISBN 978-952-60-4935-9
ISBN 978-952-60-4936-6 (pdf)
ISSN-L 1799-4934
ISSN 1799-4934
ISSN 1799-4942 (pdf)

Aalto University
School of Science
Department of Applied Physics
www.aalto.fi

BUSINESS + ECONOMY

ART + DESIGN + ARCHITECTURE

SCIENCE + TECHNOLOGY

CROSSOVER

DOCTORAL DISSERTATIONS